

석사 학위논문
Master's Thesis

고충실도 표면 법선 벡터 측정을 위한
다분광 포토메트릭 스테레오 시스템 개발

Developing a Multispectral Photometric Stereo System
for Acquiring High-Fidelity Surface Normals

남길주 (南吉柱 Nam, Giljoo)
전산학과
Department of Computer Science

KAIST

2014

고충실도 표면 법선 벡터 측정을 위한
다분광 포토메트릭 스테레오 시스템 개발

Developing a Multispectral Photometric Stereo System
for Acquiring High-Fidelity Surface Normals

Developing a Multispectral Photometric Stereo System for Acquiring High-Fidelity Surface Normals

Advisor : Professor Kim, Min Hyuk

by

Nam, Giljoo

Department of Computer Science

KAIST

A thesis submitted to the faculty of KAIST in partial fulfillment of the requirements for the degree of Master of Science in the Department of Computer Science. The study was conducted in accordance with Code of Research Ethics¹.

2014. 6. 18.

Approved by

Professor Kim, Min Hyuk

[Advisor]

¹Declaration of Ethical Conduct in Research: I, as a graduate student of KAIST, hereby declare that I have not committed any acts that may damage the credibility of my research. These include, but are not limited to: falsification, thesis written by someone else, distortion of research findings or plagiarism. I affirm that my thesis contains honest conclusions based on my own careful research under the guidance of my thesis advisor.

고충실도 표면 법선 벡터 측정을 위한 다분광 포토메트릭 스테레오 시스템 개발

남길주

위 논문은 한국과학기술원 석사학위논문으로
학위논문심사위원회에서 심사 통과하였음.

2014년 6월 18일

심사위원장 김민혁 (인)

심사위원 박진아 (인)

심사위원 윤성의 (인)

MCS

20124396

남길주. Nam, Giljoo. Developing a Multispectral Photometric Stereo System for Acquiring High-Fidelity Surface Normals. 고충실도 표면 법선 벡터 측정을 위한 다분광 포토메트릭 스테레오 시스템 개발. Department of Computer Science. 2014. 54p. Advisor Prof. Kim, Min Hyuk. Text in English.

ABSTRACT

Multispectral imaging has become more accessible as an advanced imaging technique for a physically-meaningful imaging spectroscopy, and photometric stereo has been commonly practiced for digitizing a 3D shape with simplicity for more than three decades. However, these two imaging techniques have rarely been combined as 3D imaging applications yet. Reconstructing the shape of a 3D object using photometric stereo is still challenging due to optical phenomena such as global illumination, specular reflection and self shadow. In addition, removing interreflection in photometric stereo is a traditional chicken-and-egg problem as we need to account for interreflection without knowing geometry. In this thesis, we present a novel multispectral photometric stereo method that allows us to remove interreflection on diffuse materials using multispectral reflectance information. We demonstrate several benefits of our multispectral photometric stereo method such as removing interreflection and reconstructing the 3D shapes of objects to a high accuracy.

Contents

Abstract	i
Contents	ii
List of Tables	iv
List of Figures	v
1 Introduction	1
1.1 Motivation	1
1.2 Scope	2
1.3 Contributions	3
1.4 Thesis Outline	3
2 Background	4
2.1 Radiometry	4
2.2 Rendering Equation	5
2.3 Photometric Stereo	7
2.4 Shape from Normal Map	7
3 Related Work	9
3.1 Multispectral Imaging	9
3.1.1 Bandpass Filter-Based Imaging	9
3.1.2 Dispersion-Based Imaging	9
3.1.3 Multiplexing Spectral Imaging	10
3.2 Removing Interreflection in Photometric Stereo	10
3.2.1 Active Approach Using Structured Light	10
3.2.2 Interreflection Models	11
4 Multispectral Photometric Stereo	12
4.1 Multispectral Interreflection Removal	12
4.2 A Multispectral Photometric Stereo System	13
4.2.1 Multispectral Imager	14
4.2.2 Photometric Lighting System	16
4.3 System Calibration	16
4.3.1 Radiometric Calibration	16
4.3.2 Geometric Calibration	17
4.4 Experimental Procedure	19

4.4.1	Capturing a Multispectral Image	19
4.4.2	Multispectral Interreflection Removal	20
4.4.3	Photometric Stereo and Shape Reconstruction	20
5	Results	23
5.1	Separating Direct and Indirect Illumination	23
5.2	Accuracy in Acquiring a 3D Shape	26
5.3	Scanning 3D Objects	29
6	Discussion and Future Work	37
7	Conclusion	39
Appendix A	Calibration Data	41
A.1	X-rite Mini ColorChecker	41
A.1.1	Spectroradiometer	41
A.1.2	Multispectral Camera	43
Appendix B	Multispectral Images	45
B.1	A Soap	45
	References	52
	Summary (in Korean)	55

List of Tables

5.1	Inter-Comparison Using an L-shaped Object	29
5.2	Intra-Comparison Using an L-shaped Object	29
A.1	Colorchecker Radiance #1 - #12	41
A.2	Colorchecker Radiance #13 - #24	42
A.3	Colorchecker Camera Intensity #1 - #12	43
A.4	Colorchecker Camera Intensity #13 - #24	44

List of Figures

2.1	Radiometry Fundamentals	5
2.2	Geometric Relationship in a Curved Surface	6
2.3	A Surface Normal Vector and Orthographic Projection	8
4.1	LCTF Transmittance Measurement	14
4.2	Multispectral Channel Separation	15
4.3	Experimental Setup	16
4.4	Geometric Calibration of Light Sources	17
4.5	Radiometric Camera Calibration	18
4.6	Multispectral Interreflection Removal	21
4.7	Experimental Procedure	22
5.1	Direct and Indirect Illumination Separation with Happy Buddha	24
5.2	Direct and Indirect Illumination Separation with Max Planck	25
5.3	Interreflection Removal on L-shaped Object	27
5.4	Quantitative Evaluation of Our System Using an L-shaped Object	28
5.5	An Orange	30
5.6	A Plaster Figure of Mars	31
5.7	A Plaster Figure of David	32
5.8	A Soap	34
5.9	A Human Face #1	35
5.10	A Human Face #2	36
B.1	A Multispectral Image: A Soap with Light #1	45
B.2	Multispectral Reflectance: A Soap with Light #2	46
B.3	Multispectral Reflectance: A Soap with Light #3	47
B.4	Multispectral Reflectance: A Soap with Light #4	48
B.5	Multispectral Reflectance: A Soap with Light #5	49
B.6	Multispectral Reflectance: A Soap with Light #6	50
B.7	Interreflection Removal: A Soap	51

Chapter 1. Introduction

1.1 Motivation

Commodity cameras, such as DSLRs or webcams, have trichromatic channels, i.e., red, green and blue. In fact, the trichromatic sensing mechanism of such cameras is an imitation of the human visual system. Each spectral bandwidth of three channels, red, green and blue, roughly corresponds to that of long, middle and short cone of a human retina. In such a way, these cameras reproduce colors in the real world plausibly. Color, however, is a perceptual phenomenon which occurs within our brain rather than a physical/optical phenomenon. Trichromatic cameras therefore might not be suitable for physically-meaningful measurements of optical radiance due to the wide sensing bandwidth of each channel, yielding metamerism.

For this reason, multispectral imaging has been practiced for physically-meaningful measurements of radiance as an image, so-called imaging spectroscopy. In contrast to the commodity trichromatic camera, a multispectral camera yields the multiple channels of spectral power distributions of a surface as a stack of 2D images. The spectral resolution of the system, how narrow the bandwidth of each channel is and how many channels there are, varies according to the application. For example, some multispectral cameras may have 10 channels with 50 nm bandwidth, whereas some others may have 50 channels with 10 nm bandwidth. The multispectral camera has become more accessible nowadays thanks to various imaging technologies such as a liquid crystal tunable filter and a pushbroom camera. Recently, this technique has been more practiced in computer graphics and vision, military, cultural heritage, etc [16, 21, 23, 29].

Meanwhile, photometric stereo has been commonly practiced for digitizing a 3D shape with simplicity for more than three decades. Compared to other 3D scanning techniques, e.g., computed tomography (CT), magnetic resonance imaging (MRI), stereo vision, time-of-flight and 3D laser profiling, photometric stereo estimates the surface gradients of an object using multiple images taken under different lighting conditions. Although it is possible to calculate the surface gradient of an object by using other 3D scanning techniques, photometric stereo in general yields more accurate surface gradients with higher spatial resolution. Thus, photometric stereo can be used when we need to capture the high frequency geometric information of an object, e.g., inspecting the defects of manufactured products, digitizing a cultural heritage for conservation, or scanning the human skin.

While stereo vision estimates the depth information using two cameras with static illumination, photometric stereo estimates the surface normal information using a single camera with varying lighting

conditions. Using multiple images taken under a static view point but varying light directions, photometric stereo uses the shading information which varies according to the light directions. It assumes a perfect diffuse reflection, the Lambertian reflection, which means the reflected radiance solely depends on the angle between the surface normal vector and the incident light direction vector. However, the perfect diffuse reflection of a light is hard to occur in the real world due to many optical phenomena such as specular reflection, self shadows and global illumination. These obstacles degrade the accuracy of the shape measured by photometric stereo.

Since photometric stereo was introduced [3], many researchers worked on reconstructing surface normals from non-Lambertian reflections by removing self shadows and specular reflections in photometric stereo [2, 5, 10, 28, 30, 32]. Removing the global illumination effect in photometric stereo [19, 25], however, has been less discussed. Interreflection is one of the most common effects of global illumination. This effect occurs when two points over a concave surface face to each other. Most photometric stereo algorithms are designed in the general assumption of Lambertian reflection on convex shapes, which do not suffer from interreflection. However, objects in the real world are built with a mixture of convex and concave shapes.

Removing interreflection is challenging as the effect is integrated in a light path. The second-bounded light is affected by the surface albedo of the reflecting surface. The second-bounded light becomes a new light source and the reflection is added on each point. Most of energy that comes into the camera is either direct from the light source or first-bounded light from the object surface, which is the inner product of the light and surface reflectance. The portion of second and higher-bounded light varies from the scene. Some object or scene are more vulnerable to the global illumination. In this case, the radiance measured by a camera is affected by not only the illumination and the surface albedo, but also the reflectance of the surrounding surfaces.

1.2 Scope

While the two advanced imaging techniques, photometric stereo and multispectral imaging, have been developed for physically-meaningful measurements of the real world information, they have been rarely practiced together in multispectral imaging and computer vision domains. In this thesis, we combine the two techniques in order to acquire high-fidelity surface normals without suffering from interreflection. We present a novel system for removing interreflection: *multispectral photometric stereo system*.

We model the multiple bounces of *wavelength-dependent* interreflection as a polynomial function and optimize the interreflection effect through multispectral reflectance analysis. This allows us to separate interreflection over diffuse surfaces from measured radiance. Our multispectral photometric stereo does not rely on multiplexing spectral lights [29, 31], i.e., our proposed method works on arbitrary shape and illumination without help of structured or colored lights. Our interreflection removal method can be easily

integrated into existing photometric stereo systems even with a commodity trichromatic camera, albeit less powerful, while not modifying light sources. We demonstrate the usefulness of our multispectral photometric stereo to measure the shape of 3D solid objects to a high accuracy.

1.3 Contributions

The following contributions have been made through this thesis:

- **A multispectral photometric stereo system.** We design a multispectral photometric stereo system with a full description of radiometric calibration of each optical component and geometric calibration of the lighting system.
- **Interreflection removal using multispectral reflectance analysis.** We remove interreflection from the measured radiance using multispectral reflectance analysis in order to estimate the shape of an object to a high accuracy.
- **A passive method to remove interreflection.** Our passive method to remove interreflection which does not need to modify the light source, e.g., structured light or colored light, enables our method to be integrated easily into an existing photometric stereo system by replacing the camera with a multispectral camera.

1.4 Thesis Outline

The rest of this thesis is organized as follows. Chapter 2 presents the background knowledge for understanding the technical details in this thesis. In Chapter 3, we present previous work on multispectral imaging and interreflection removal in photometric stereo. Chapter 4 describes the details on our multispectral photometric stereo system and interreflection removal method. The experimental results as well as the evaluation of our method are presented in Chapter 5. Chapter 6 summarizes this thesis and discusses the main contributions and future work as well as the limitation of our method. Finally, Chapter 7 concludes this thesis. Appendices A and B provide the experimental data.

Chapter 2. Background

In this chapter, we provide background knowledge that is necessary to understand the remaining part of this thesis. We first explain the radiometry fundamentals, such as radiance and Lambertian reflection, followed by the rendering equation. Then we describe estimating surface normals and the 3D shape of an object using photometric stereo.

2.1 Radiometry

Light is electromagnetic radiation which is visible to the human visual system, of which the spectrum extends from 380 nm to 780 nm. In other words, light is electromagnetic radiation which the human visual system can sense. The goal of this thesis is to model and manipulate the physical light transport in the real world, i.e., global illumination. To this end, we need to understand the physical quantities of light energy. In general, there are two ways to represent light energy: radiometry and photometry. Photometry deals with the perception of light. It takes accounts for the sensitivity of the human visual system with regard to the light energy. In contrast, radiometry accounts for the physical quantification of the light energy. As our goal is to model the physical light transport, i.e., global illumination, we use the radiometric terms throughout this thesis.

Since light is electromagnetic radiation, light has its own energy: *radiant power* or *flux* $[\Phi, W]$. Radiant power is the fundamental quantity in radiometry. It accounts for the total energy that leaves from or arrives at a surface per unit time. For a scientific purpose, we use another radiometric quantity, *irradiance*. Irradiance expresses the radiant power of incident light per unit surface area $[d\Phi/dA, W/m^2]$. *Radiance* is a radiant power per unit surface area per solid angle $[d^2\Phi/d\omega dA, W/m^2 \cdot sr]$. We use the notation $L(x \rightarrow \Theta)$ to indicate the radiance on a point x toward a certain direction Θ . When we measure the energy of light through an optical system, such as the human visual system or a camera, we measure the radiance of the light. In other words, such optical systems have a sensor response proportional to the radiance and it is the radiance that determines the appearance of an object when we capture it with our imaging system. For this reason, radiance is the most important radiometric quantity in this thesis.

If the outgoing radiance determines the appearance of an object, what determines the outgoing radiance? Traditionally, a bidirectional reflectance distribution function (BRDF) has been used to represent the material appearance in the field of optics and computer graphics. The BRDF is a four-dimensional function that accounts for the ratio between the incident irradiance and the reflected radiance

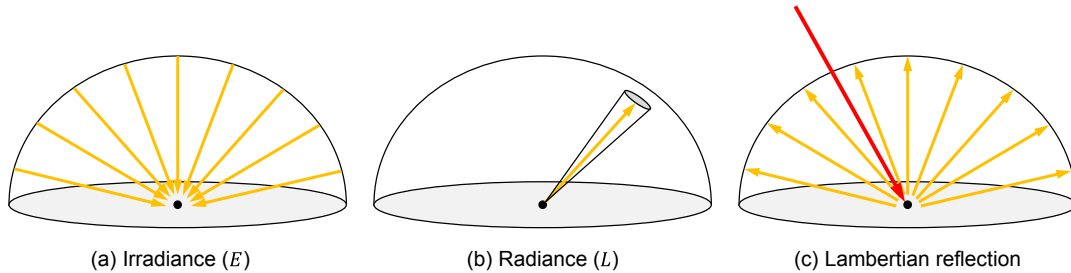


Figure 2.1: *Radiometry fundamentals. (a) Irradiance is incident radiant power per unit surface area. (b) Radiance is radiant power per unit surface area per solid angle. (c) Lambertian reflection means that the reflected radiance is constant over the hemisphere.*

per pixel. The BRDF can be express as

$$f_r(x, \Psi \rightarrow \Theta) = \frac{dL(x \rightarrow \Theta)}{dE(x \leftarrow \Psi)}, \quad (2.1)$$

where Ψ and Θ are the incident and reflected light direction vectors, and $dE(x \leftarrow \Psi)$ and $dL(x \rightarrow \Theta)$ are the differentials of the incident irradiance and the reflected radiance, respectively.

Diffuse materials, such as papers or plasters, reflect the incident light with Lambertian reflection. Lambertian reflection indicates that the BRDF of a surface is constant for every incident direction Ψ and reflected direction Θ . That is, $f_r(x, \Psi \rightarrow \Theta) = \rho(x)/\pi$, where $\rho(x)$ is the diffuse reflectance of the surface. For the Lambertian reflection, the outgoing radiance can be expressed in a simpler manner: $L(x \rightarrow \Theta) = L(x)$.

2.2 Rendering Equation

The rendering equation [14] is one of the most important equations in computer graphics. The equation enables us to generate virtual, but physically correct, images with computer graphics techniques. In this thesis, we utilize the equation in an inverse manner: to reconstruct a 3D shape from the estimated radiance, not to create an image.

When a beam of light strikes a diffuse surface of a color, some light is scattered backward as well as to neighboring surfaces. Iterative scattering occurs between neighboring surfaces, and we call this phenomenon *interreflection*. Interreflection always occurs along the surface when a concave shape is illuminated.

When a light source L_e illuminates a surface point x , we can model the light from a viewing direction Θ as below:

$$L(x \rightarrow \Theta) = L_e(x \rightarrow \Theta) + L_r(x \rightarrow \Theta). \quad (2.2)$$

Here the reflected light is often modeled as an integration over a hemisphere Ω [14]:

$$L_r(x \rightarrow \Theta) = \int_{\Omega_x} f_r(x, \Psi \rightarrow \Theta) L(x \leftarrow \Psi) \cos(N_x, \Psi) d\omega_\Psi, \quad (2.3)$$

where $f(x, \Psi \rightarrow \Theta)$ is a BRDF and can be simplified as $\rho(x)/\pi$ for Lambertian surfaces; N_x is the surface normal vector at the point x . In order to specify the geometric relationship between the illuminated and reflecting surfaces, we transform the spherical domain of the integration of Eq. (2.3) to the surface domain:

$$L_r(x) = \frac{1}{\pi} \int_A \rho(x) L(y) V(x, y) G(x, y) dA_y, \quad (2.4)$$

where $V(x, y)$ is a binary visibility function, which determines if the surface x is visible from the surface y and $G(x, y)$ defines the geometrical relationship between the illuminating surface y and the reflected surface x along the direction Ψ at a distance r_{xy} : $V(x, y) = \frac{\Psi \cdot N_x + |\Psi \cdot N_x|}{2|\Psi \cdot N_x|} \frac{-\Psi \cdot N_y + |-\Psi \cdot N_y|}{2|-\Psi \cdot N_y|}$, $G(x, y) = \cos(N_x, \Psi) \cos(N_y, -\Psi) / r_{xy}^2$. Let's denote $V(x, y)G(x, y)$ as $K(x, y)$, so-called a *form factor*, which accounts for the geometrical relationship w.r.t. the interreflection effect. Fig. 2.2 illustrates these geometrical relationship in the case of a curved surface.

We can substitute Eq. (2.2) with Eq. (2.4) and simplify it in a discrete matrix-vector form:

$$L = L_e + (\rho K)L, \quad (2.5)$$

where L is a radiance vector of each infinitesimal patch dA , L_e is a self-emitting radiance vector of each patch as a light source, and ρK is a matrix that determines how much light energy is transferred among the patches. Assuming a state of equilibrium for light transfer, we can rewrite Eq. (2.5) as below:

$$L = (I - \rho K)^{-1} L_e. \quad (2.6)$$

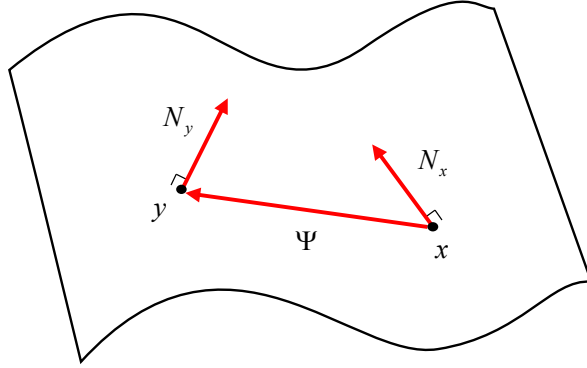


Figure 2.2: Geometric relationship in a curved surface. Interreflection always occurs when two points over a concave surface face to each other. The form factor $K(x, y)$ accounts for the geometric relationship between the two facing points. N.B. $K(x, y)$ is also called as ambient occlusion in rendering techniques.

Again we can expand Eq. (2.6) into a Neumann series:

$$L = L_e + (\rho K)L_e + (\rho K)^2 L_e + \dots + (\rho K)^n L_e. \quad (2.7)$$

In this form, we can easily model how much light energy is contributed from n -bounded light; the n -th order of the polynomial is equivalent to the effect of n -bounded light. This allows us to remove indirection illumination from the measured radiance. Refer to the work by Koenderink and Van Doorn [17] and Yu et al. [33] for more details on modeling interreflection.

2.3 Photometric Stereo

Once we remove the indirect illumination from reflection, we compute surface normals using direct reflections by a set of individual point lights in photometric illumination. A shading illuminated by a point light can be calculated by simplifying the reflection equation (Eq. (2.3)) as a dot product:

$$I = L \cdot \bar{N},$$

where I is a reflected light; L is a column vector of direct illumination radiance scaled by the reflectance ρ ; \bar{N} is a surface normal vector. Suppose we obtain i images under different lighting directions in photometric illumination, we can obtain the following linear system for each point on the surface:

$$\begin{bmatrix} I_1 \\ I_2 \\ \vdots \\ I_i \end{bmatrix} = \begin{bmatrix} L_{1,x} & L_{1,y} & L_{1,z} \\ L_{2,x} & L_{2,y} & L_{2,z} \\ \vdots & \vdots & \vdots \\ L_{i,x} & L_{i,y} & L_{i,z} \end{bmatrix} \begin{bmatrix} \bar{N}_x \\ \bar{N}_y \\ \bar{N}_z \end{bmatrix}. \quad (2.8)$$

To solve the linear system above, the row-rank of the matrix \mathbf{L} should be at least three, i.e., we need at least three point lights. If more than three light sources are used, it becomes an over-constrained linear system, which can be solved by a least-square optimization method. Once we obtain \bar{N} , normalizing it yields a surface normal vector N for each point.

2.4 Shape from Normal Map

Once we obtain a surface normal per pixel, we can recover a 3D shape (a set of $\{x, y, z\}$) of the object [3]. By definition, a surface normal is orthogonal to the tangential plane. Assuming an orthographic projection

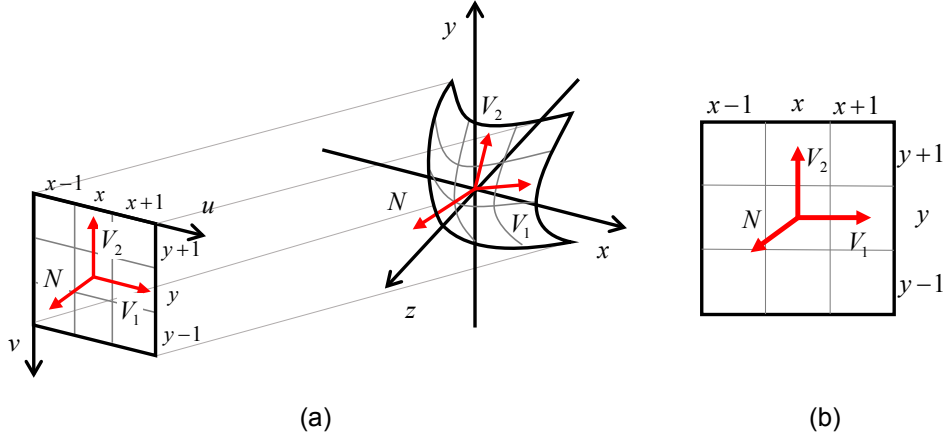


Figure 2.3: A surface normal vector and orthographic projection. (a) shows orthographic projection of a surface normal vector and its tangential vectors. (b) shows the projected vectors on an image plane. Based on orthographic projection, we can approximate the tangential vectors as $V_1 = [1, 0, z_{(x+1,y)} - z_{(x,y)}]^T$ and $V_2 = [0, 1, z_{(x,y+1)} - z_{(x,y)}]^T$

(See Fig. 2.3), we can make the following constraints.

$$\begin{aligned} N \cdot V_1 &= 0; \\ N \cdot V_2 &= 0, \end{aligned} \tag{2.9}$$

where N is a surface normal vector ($N = [N_x, N_y, N_z]^T$), and V_1 and V_2 are two surface tangential vectors along x and y directions respectively ($V_1 = [1, 0, z_{(x+1,y)} - z_{(x,y)}]^T$, $V_2 = [0, 1, z_{(x,y+1)} - z_{(x,y)}]^T$).

Rewriting Eq. (2.9) yields:

$$\begin{aligned} z_{(x+1,y)} - z_{(x,y)} &= -N_x/N_z; \\ z_{(x,y+1)} - z_{(x,y)} &= -N_y/N_z. \end{aligned} \tag{2.10}$$

Now we can reconstruct the height field z at (x, y) by minimizing the following objective function:

$$\Gamma(z) = \sum_{x,y} \left(N_z \frac{\partial z(x,y)}{\partial x} + N_x \right)^2 + \left(N_z \frac{\partial z(x,y)}{\partial y} + N_y \right)^2, \tag{2.11}$$

where the partial derivatives of z to x and y are as below:

$$\begin{aligned} \frac{\partial z(x,y)}{\partial x} &= z(x+1,y) - z(x,y); \\ \frac{\partial z(x,y)}{\partial y} &= z(x,y+1) - z(x,y). \end{aligned} \tag{2.12}$$

Minimizing Eq. (2.11) yields a set of $\{x, y, z\}$, the 3D geometry of the object in a 3D coordinate.

Chapter 3. Related Work

This section briefly overviews relevant previous work in multispectral imaging and removing interreflection in photometric stereo.

3.1 Multispectral Imaging

Multispectral imaging is often called as imaging spectroscopy, where a pixel in a spectral image indicates spectral power per wavelength to present spatial variation of spectrum on captured radiance. Bandpass filters [1, 27, 29] or a dispersion unit [6, 9, 15, 16, 24] are commonly employed to build a multispectral imaging system.

3.1.1 Bandpass Filter-Based Imaging

A bandpass filter-based imaging system includes a set of narrow bandpass filters on a wheel [27], or a liquid crystal tunable filter (LCTF) [1] in its optical path. A monochromatic sensor captures the energy of a certain frequency band through a bandpass filter, where the spectral resolving power depends on the bandwidth of the filter. While the minimum bandwidth of a general optical filter is about 10–15 nm, the minimum bandwidth of an LCTF is about 7–10 nm. In this thesis, we use a multispectral camera, of which the monochromatic sensor is coupled with an LCTF. Recently, Lee and Kim [18] used two LCTFs, one for visible spectrum light and one for near infrared spectrum light, to build a two-way hyperspectral imager with a high spatial resolution. Takatani et al. [29] introduced a photometric stereo method using multispectral imaging with nine bandpass filters. They enhanced the accuracy of estimated surface normals by segmenting multispectral image data and identifying a wavelength per segment patch that fits the most to the Lambertian constraints. They mainly focused on searching optimal spectral wavelength to represent Lambertian reflection and did not concern the interreflection effect while reconstructing the normals. In contrast, our work investigates the nature of wavelength-dependency from multispectral channels with respect to interreflection.

3.1.2 Dispersion-Based Imaging

Pushbroom-based imaging system is a type of the common imaging systems based on the dispersion effect. The pushbroom camera includes a slit and a dispersion unit such as a prism [24]. The camera measures the dispersed spectrum of the light from a single column of the imager via the slit. One of

the shortcomings of this approach is that the system needs to move the sensor or the slit mechanically. The spatial resolution of the spectral images in the mechanical moving direction is lower than the other direction. Recently, two-dimensional dispersion-based systems have been introduced [6, 9, 16]. These techniques are based on the compressive sensing technique. As a sensor with a compressive mask captures dispersion as an image entirely, these systems are capable of recording a multispectral video of moving objects. However, the spatial resolution has been significantly lower than the pushbroom-based ones. Improving its spatial resolution has been researched actively [15].

3.1.3 Multiplexing Spectral Imaging

Multiplexing of narrow-band spectra is an alternative for multispectral imaging. A series of narrow-band LED lights in general is coupled with a monochromatic camera. This configuration enables to capture multispectral reflection from the multispectral light source. Recently Vogiatzis and Hernandez [31] introduced a multiplexing-light based photometric stereo method that allows to capture 3D animation using a structure-from-motion approach. Brostow et al. [4] also reconstructed a 3D video sequence using photometric stereo with trichromatic multiplexed lights.

3.2 Removing Interreflection in Photometric Stereo

Photometric stereo, also known as *shape-from-shading*, estimates surface gradients using images taken under multiple light directions, assuming that the surface reflection observes the Lambertian constraints. As interreflection breaks this assumption, which is critical for photometric stereo, there has been a few work on removing interreflection in photometric stereo.

3.2.1 Active Approach Using Structured Light

Nayar et al. [26] introduced a seminal work to remove interreflection using structured light patterns. They used a high frequency illumination pattern in order to separate the direct and global illuminations of a scene. While two illumination patterns are enough to separate the global illumination theoretically, three illumination patterns were used in practice. For photometric stereo, they used the high frequency illumination patterns for each light source; thus at least triple-number of images were required. Gupta and Nayar [8] and Gu et al. [7] utilized the global illumination separation technique in [26]. Gupta and Nayar [8] presented micro phase shifting technique, i.e., sinusoidal illumination patterns with narrow band and high frequency. They reduced the number of illumination patterns needed for shape recovery using the micro phase shifting. By using only narrow band and high frequency patterns, the global illumination effects become the same for every image under each illumination pattern; thus they could remove the

global illumination effects (similar to dark-noise removal). Gu et al. [7] reduced the required number of illumination patterns by using multiplexing the illumination. By using multiplexed illumination, Gu et al. [7] also increased the signal-to-noise ratio of input images.

3.2.2 Interreflection Models

Nayar and Kanade [25] presented an iterative method to estimate non-biased surface normals. They first estimated a pseudo shape, a shape that contains interreflection in its shape and reflectance, and iteratively corrected the pseudo shape so that it converges to the real shape. They also showed the convergence property of their iterative algorithm. Liao et al. [19] presented an active method to remove n -bounded light in photometric stereo using colored multiplex lighting. The proposed algorithm theoretically assumes that there are at least two images of an object with same illumination but varying surface albedos. However, this assumption is technically impossible in the real world. Instead, they changed the illumination spectrum to emulate the changes of surface albedo. They modeled and solved an interreflection model based on monochromatic surface albedo.

Most of prior interreflection-removal methods either have taken iterative method or have employed active approaches with the specially designed illumination patterns or the colored light sources. In contrast, we propose a channel separation technique in multispectral imaging without relying on an active lighting approach or an iterative method. Therefore, our passive method can be easily integrated into any previous photometric stereo systems and remote sensing systems.

Chapter 4. Multispectral Photometric Stereo

Our objective is to separate direct reflection from global illumination in order to reconstruct high-fidelity surface normals and geometry using photometric stereo from multispectral image data. This section describes the technical details.

4.1 Multispectral Interreflection Removal

The technical insight of our multispectral photometric stereo is that the interreflection of n -bounded light increases reflected energy consistently as an n -th order polynomial function of reflectance ρ along the wavelength. Using Eq. (2.7), we can rewrite the reflection equation (Eq. (2.4)) as a polynomial function of reflectance ρ :

$$L_r = \rho K L_e + (\rho K)^2 L_e + \dots + (\rho K)^n L_e, \quad (4.1)$$

where K is the form factor of the product of the visibility V and the cosine term G . Now distinguishing direct/indirect illumination from reflection is equivalent to identifying each term of the polynomial. If we measure the radiance L_r multiple times assuming constant K but varying L_e and ρ values, we can get a linear system for the variables L_e and ρ . By solving the linear system, we can distinguish direct/indirect illumination. Liao et al. [19] conducted a seminal experiment and proved this mathematics using ray tracing rendering. However, it is prohibitively demanding to take the images of the same object with different reflectance values while maintaining the geometry in the real world. Liao et al. [19] solved this problem by illuminating a monochromatic surface with an RGB projector, thus simulating the varying surface reflectance effect.

In contrast to Liao et al. [19], we do not change the spectrum of the light source. Thus, off-the-shelf lighting bulbs, e.g., LED lamps, are sufficient for the interreflection-free photometric stereo setup in our method. Furthermore, we use narrow bandwidth (about 10 nm to 20 nm) which can distinguish metameric colors. We mainly benefit from the fact that most materials in the real world have different reflectances in different wavelengths, except for a Spectralon tile. We treat each wavelength channel as an independent observation with different illumination and reflectance respectively. This allows us to distinguish n -bounded light using multiple observation of individual multispectral channels of the same surface without relying on multiplexing of light or albedo [19]. Now we can extend Eq. (4.1) as a series of

n -order polynomials with multispectral channels λ :

$$\begin{aligned}
L_1 &= \rho_1 L_{e,1} K + \rho_1^2 L_{e,1} K^2 + \cdots + \rho_1^n L_{e,1} K^n \\
L_2 &= \rho_2 L_{e,2} K + \rho_2^2 L_{e,2} K^2 + \cdots + \rho_2^n L_{e,2} K^n \\
&\vdots \\
L_\lambda &= \rho_\lambda L_{e,\lambda} K + \rho_\lambda^2 L_{e,\lambda} K^2 + \cdots + \rho_\lambda^n L_{e,\lambda} K^n,
\end{aligned} \tag{4.2}$$

We can rewrite Eq. (4.2) as a linear system equation:

$$\begin{bmatrix} L_1 \\ L_2 \\ \vdots \\ L_\lambda \end{bmatrix} = \begin{bmatrix} L_{e,1}\rho_1 & L_{e,1}\rho_1^2 & \cdots & L_{e,1}\rho_1^n \\ L_{e,2}\rho_2 & L_{e,2}\rho_2^2 & \cdots & L_{e,2}\rho_2^n \\ \vdots & \vdots & \ddots & \vdots \\ L_{e,\lambda}\rho_\lambda & L_{e,\lambda}\rho_\lambda^2 & \cdots & L_{e,\lambda}\rho_\lambda^n \end{bmatrix} \begin{bmatrix} K \\ K^2 \\ \vdots \\ K^n \end{bmatrix}, \tag{4.3}$$

It is worth noting that the spectral profile of illumination L_e is multiplied with the reflectance polynomials ρ . We can obtain these two properties from the multispectral imaging system. Now let's simplify it in a matrix-vector form:

$$L = \mathbf{R}A, \tag{4.4}$$

where L is a multispectral radiance vector; \mathbf{R} is an element-wise multiplication of the illumination and the reflectance polynomials; A is a vector of polynomials of form factors. To solve the Eq. (4.4), we calculate A by minimizing the following objective function $O(A)$:

$$O(A) = \|L - \mathbf{R}A\|_2^2. \tag{4.5}$$

In our system, the row-rank of λ (e.g., 29 channels) is higher than n (the order of bounce). It becomes an over-constrained linear system, which can be solved by a general least-squares optimization method such as QR decomposition or SVD. Although our method in theory can solve the same order of bounce as the number of the multispectral channels, we cut off the terms higher than n because they are physically and numerically negligible in our experiment.

4.2 A Multispectral Photometric Stereo System

Our imaging system comprises two main folds: a multispectral imager and a photometric lighting system with six LED lights. In this section, we describe each part of our multispectral photometric stereo system and illustrate the full system calibration procedure.

4.2.1 Multispectral Imager

We first build a multispectral imager, which consists of an LCTF (Varispec VIS0720), a monochromatic camera (Point Grey FL3-GE-13S2M-C) and a Nikon F-mount lens. The monochromatic camera includes a 14-bit analog-to-digital converter (ADC). Hence, we output 16-bit RAW images so that we can make use of full performance of the sensor. We turn off gamma-correction as gamma-correction yields non-linear camera response to the incident radiance. A linear camera response is a matter of great importance in the following camera calibration process. We carefully choose the focal length of the lens to avoid the vignetting effect caused by the LCTF in front of the objective lens. In the following experiments, we used Nikon F-mount lens with 35 mm focal length. Fig. 4.1 shows the measured transmittance of the LCTF. Fig. 4.2 shows an example of radiometric measurements by our multispectral imager. (b) shows measured reflectance of a red color under the LED illumination (a). (c) shows the configuration example of the LCTF transmittance. In our method, we treat each channel as if it is an independent scene with its own irradiance and reflectance but theoretically on a same geometry, e.g., we regard a channel of 550 nm is a scene that has the same irradiance level with a channel of 650 nm and has one-tenth of reflectance than the channel of 650 nm of the same geometry.

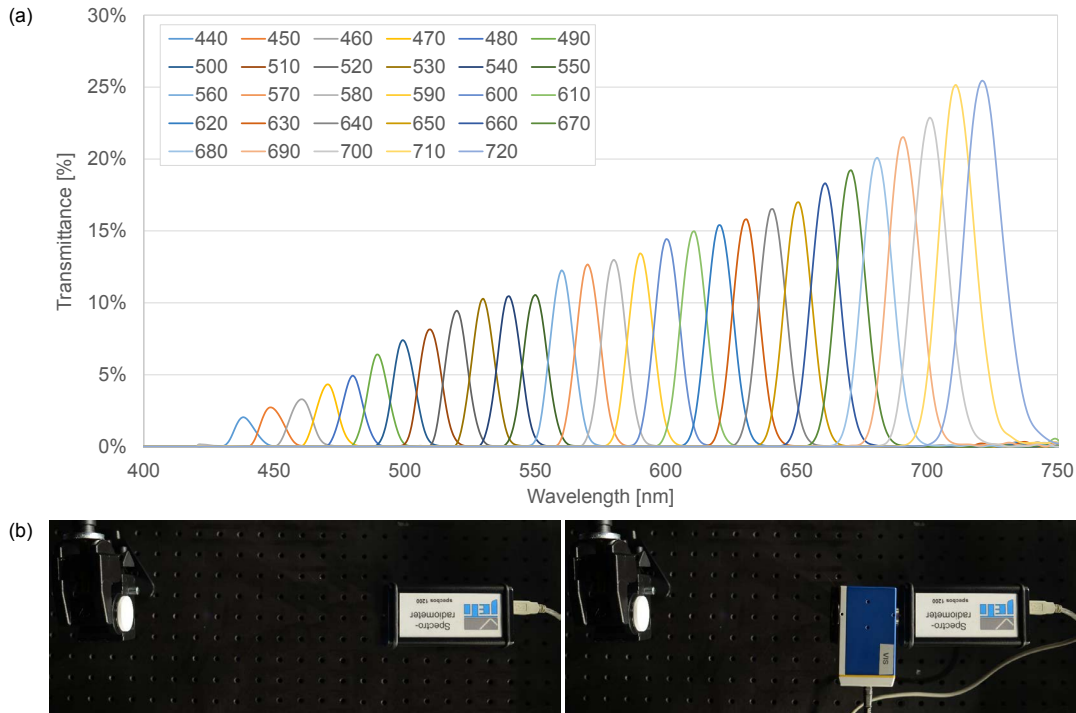


Figure 4.1: An LCTF transmittance measurement (a) shows the measured the transmittance functions of the LCTF for each wavelength, from 440 nm to 720 nm in 10 nm intervals. (b) show the measurement procedure. We measure the reflected radiance on a Spectralon with and without the LCTF. Dividing the radiance with the LCTF by the radiance without the LCTF yields the transmittance of the LCTF. A spectroradiometer (Jeti Specbos 1200) is used for the physically correct measurement of radiance.

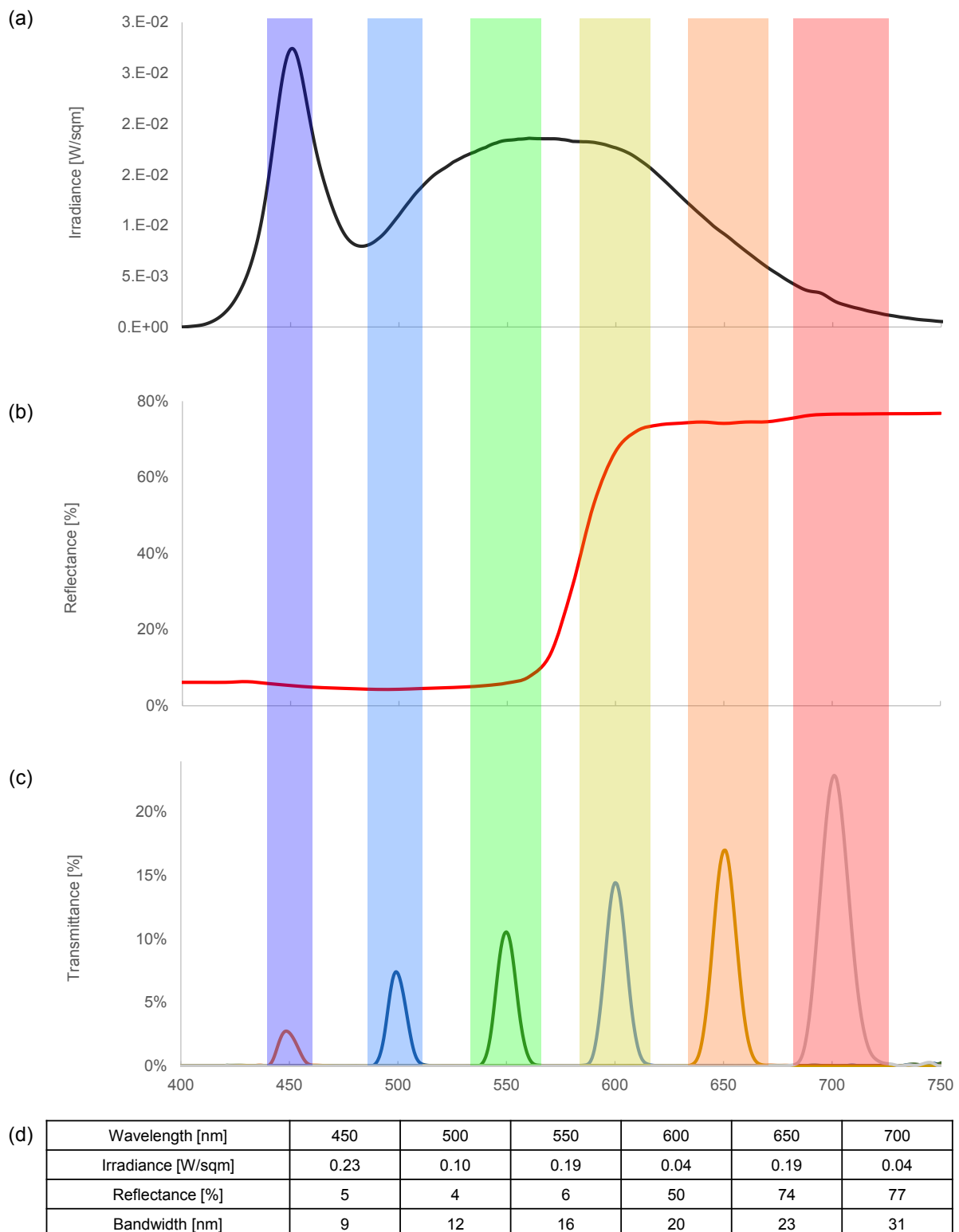


Figure 4.2: An example of radiometric measurements by our multispectral imager. (a) presents the measured irradiance of the LED lights for photometric stereo. (b) shows a reflectance example of a red patch. (c) describes the measured transmittance example in 50nm intervals of our LCTF filter. (d) compares the irradiance, reflectance, and the transmittance of the LCTF.

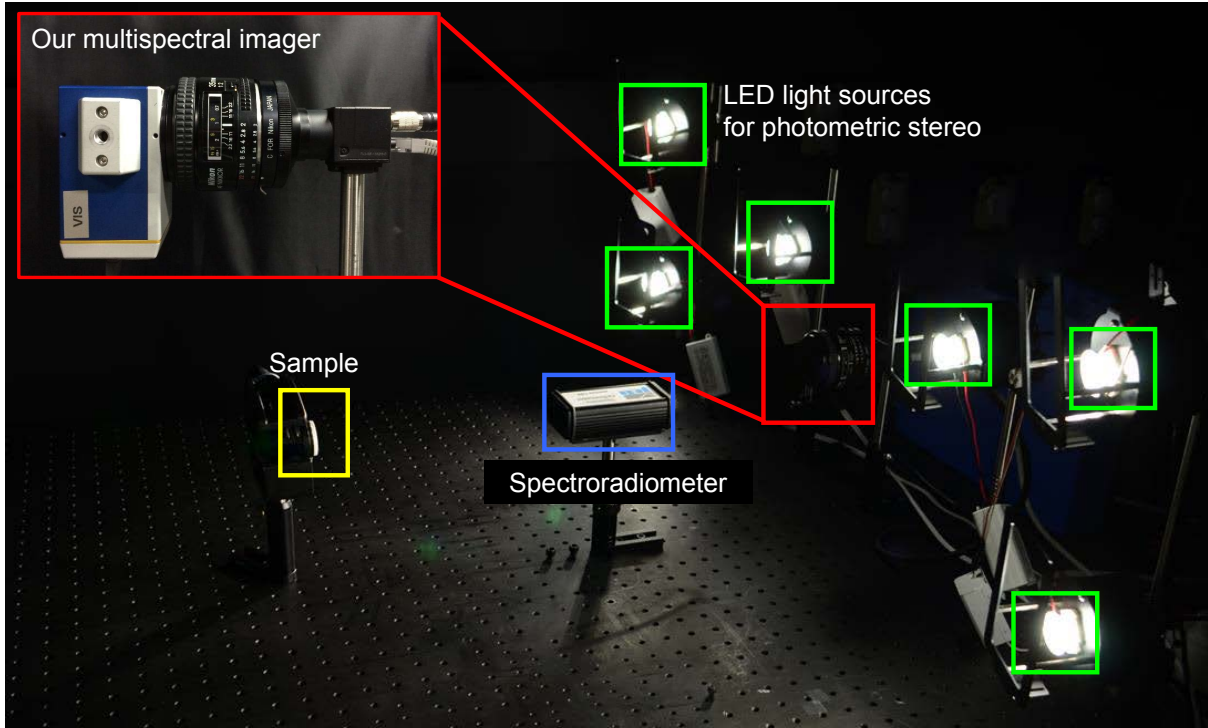


Figure 4.3: *Our multispectral photometric stereo system. We configure this imaging system with our custom-built multispectral imager and six visible LED light sources. A spectroradiometer is used for the radiometric calibration of our system.*

4.2.2 Photometric Lighting System

After we build the multispectral imager, we complete a multispectral photometric stereo system by attaching six LEDs as light sources in our system. We choose CREE CXA1512 high power LED coupled with a heat sink. The LED with heat sink provides a stable illumination, less time varying, and no peak spectrum. It is important that the light source does not have a peak spectrum since the peak spectrum may yield biased output in multispectral imaging of narrow bandwidth. The LED lights are positioned at 0.62m distant from the target object. Our system setup and multispectral filter transmittance are illustrated in Fig. 4.3 and Fig. 4.1.

4.3 System Calibration

4.3.1 Radiometric Calibration

We first calibrate our multispectral imager radiometrically in order to be capable of physically-meaningful measurements of radiance. In our multispectral imaging system, the camera sensor signal of a channel I_λ is a product of the incident radiance L_λ , the transmittance efficiency of the lens T_λ , the transmittance

function of the LCTF $F_{BAND,\lambda}$, and the quantum efficiency of the sensor Q_λ :

$$I_\lambda = Q_\lambda T_\lambda F_{BAND,\lambda} L_\lambda.$$

As we desire to estimate physically-meaningful radiance from the camera sensor signal, we determine a linear transformation C_λ , which is an inverse camera response function, $(Q_\lambda T_\lambda F_{BAND,\lambda})^{-1}$.

We use an X-rite ColorChecker with 24 color patches with known reflectances. Two LED lamps illuminate the ColorChecker at 45 degrees of both sides. A spectroradiometer (Jeti Spechbos 1200) and our multispectral camera measure the reflected radiance and the camera sensor signal respectively. We find a linear mapping function C_λ using two measurements while taking into account of the measured transmittance function of LCTF, $F_{BAND,\lambda}$. The calibration results are shown in Fig. 4.5. Once we calibrate the multispectral camera, we can measure the physically-meaningful radiance of an arbitrary scene with the camera sensor signal by multiplying C_λ , i.e., we can employ the multispectral camera functioning as a two-dimensional spectroradiometer. Measurement data of radiometric calibration are tabulated in Appendix A

4.3.2 Geometric Calibration

Geometric calibration for the position of point lights is necessary for photometric stereo. Fig. 4.4 shows our geometric calibration of the light direction vector. We place a chrome ball at the same position which the object will be placed at. The specular reflection of a point on a chrome ball (with a known diameter) indicates a reflected light R about the normal vector N . Using the symmetry of the law of reflection, we can determine the light direction L with respect to the viewing direction (same as R), solving the equation below:

$$L = 2(N \cdot R)N - R.$$

We calibrate the light vectors for all the point lights.

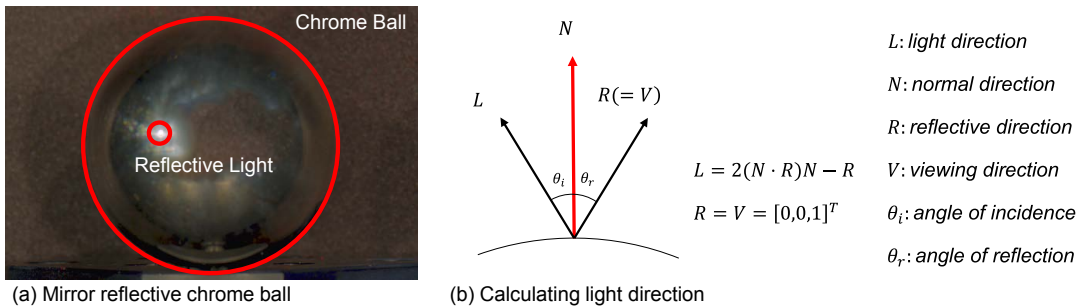


Figure 4.4: Geometric calibration of a light for photometric stereo. (a) shows the mirror reflective chrome ball used in our experiment. (b) presents calculating the light directions. The specular reflection of a point on a chrome ball indicates a reflected light about the normal vector N . Using the symmetry of the law of reflection, we can determine the light direction L with respect to the viewing direction $V (= R)$.

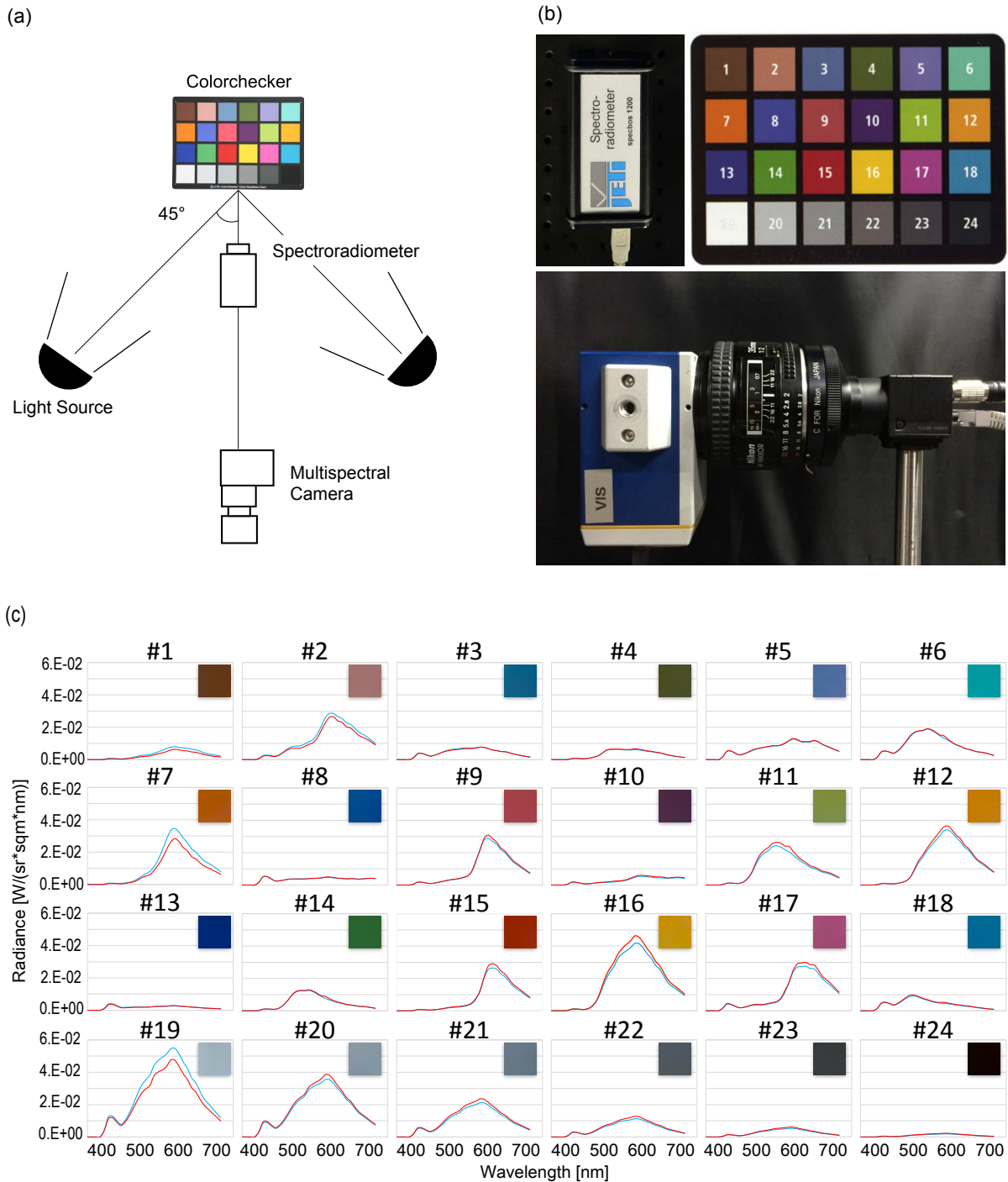


Figure 4.5: Radiometric calibration of our multispectral imager. (a) shows our measurement setup for radiometric calibration. (b) shows each component used in the calibration procedure: a spectroradiometer, an X-rite ColorChecker, and our multispectral imager. (c) presents radiance measured by our multispectral imager, compared with the measurements by a spectroradiometer. The red plot indicates the radiance measured by our system; the blue plot indicates the radiance measurement by the spectroradiometer. Coefficient of variance (CV) between two measurements among 24 color patches are just 2.2%.

4.4 Experimental Procedure

In this section, we illustrate the experimental procedure in detail. We assume that we conducted the system calibration and we already have the calibration parameters such as the inverse camera response function (C_λ) and the light direction vectors (L). The experimental procedure is as follows. First, we capture multispectral image of an object with our multispectral camera for each light source and save the multispectral images in OpenEXR format files (Section 4.2.1). Second, we perform multispectral interreflection removal for each multispectral image (Section 4.1). Third, we perform photometric stereo using interreflection-free images and get surface normal map of the object (Section 2.3). Finally, we reconstruct the 3D shape of the object using the normal map (Section 2.4). Fig. 4.6 and Fig. 4.7 show the schematic diagram of our method and the resulting 3D geometry.

4.4.1 Capturing a Multispectral Image

The very first step of our method is to capture the multispectral image of an object. We build a C++ program to capture a sequence of monochromatic images of varying spectral bands. We use the Point Grey FlyCapture SDK [12] to control the monochromatic camera. We also use the CRi VariSpec SDK [11] to control the LCTF with our program. The external parameters, such as a shutter speed of the camera or the target spectral band of the LCTF, are passed to the program through a script file.

When capturing an object, we place a Spectralon (99% calibrated) alongside the object in order to calculate the multispectral reflectance of the object. We adjust the exposure time of the camera to the reflectance of the Spectralon in the brightest channel. In this manner, we can easily calculate the reflectance of the object without any saturation effect. For the multispectral reflectance, we choose a convex area, where interreflection does not occur, and divide the mean intensity value of the area by the mean intensity value of the spectralon for each channel. We store the multispectral reflectance data of multiple channels in a multi-layer OpenEXR file.

OpenEXR was originally invented to store a high-dynamic-range (HDR) image. It can store an image data with a 16-bit half precision float type [20]. In general, OpenEXR file uses 64 bits per pixel: 4 channels for red, green, blue and alpha. OpenEXR file also provides additional channels to store 2D data. We use the additional channels to store the 2D multispectral reflectance data. Each channel stores the 2D multispectral reflectance data for the corresponding wavelength. We calculate the sRGB value per pixel using the measured multispectral radiance. We transform the multispectral reflectance data into a corresponding color in a CIE XYZ color space under D65 illumination, and again transform the color space into an sRGB color space. We fill in the RGBA channels of the OpenEXR file with the calculated sRGB value and the alpha of 1.0.

4.4.2 Multispectral Interreflection Removal

Once we obtain the multispectral reflectance of an object, we perform interreflection removal (Eq. (4.5)) and yield an image of direct reflection. We use MATLAB [22] to solve the optimization problem (Eq. (4.5)). We use the built-in function *mldivide*, a QR decomposition method. As solving Eq. (4.5) is a per-pixel operation independent to the adjacent pixels, we can parallelize the optimization using the Parallel Computing Toolbox in MATLAB.

Although we can get the direct reflection images of all the wavelength channels, we only need one direct reflection image per light source. Thus, we select a channel that has a maximum intensity, in other words, the brightest channel. The brightest channel has its advantage in a higher signal-to-noise ratio, resulting in a robust estimation of surface normal in photometric stereo. After interreflection removal, we save the monochromatic direct reflectance image per light source in a 16-bit PNG file.

4.4.3 Photometric Stereo and Shape Reconstruction

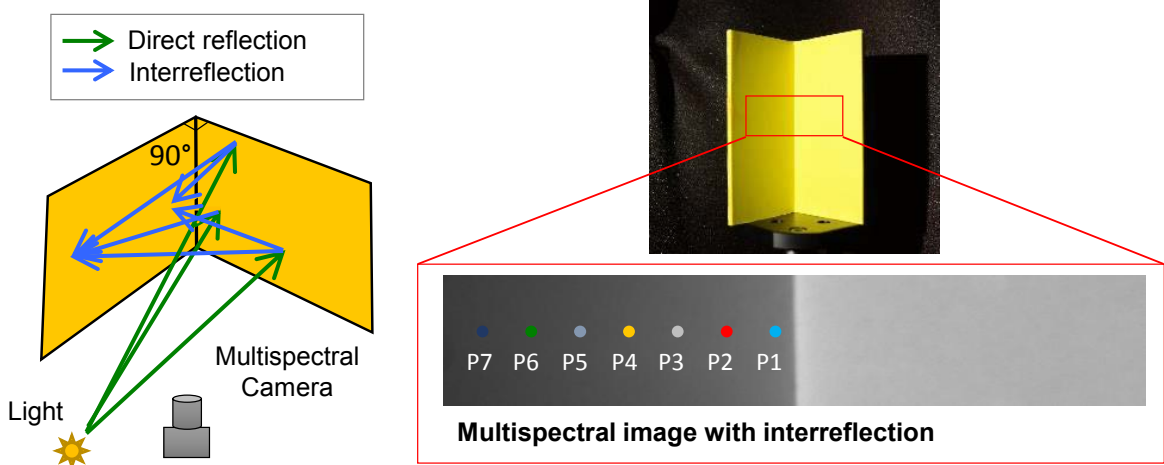
With the direct reflection images and the light direction vectors, we perform photometric stereo. Solving Eq. (2.8) with six light sources is an over-constrained linear system problem, which can be solved using the QR decomposition. We again use MATLAB to solve Eq. (2.8): *mldivide* function.

Now we reconstruct the 3D shape of the object. With Eq. (2.10) and Eq. (2.12), we can build the following over-constrained linear system (Eq. (4.6)) with regard to every $z(x, y)$ of points. Solving the linear system with least square method, we obtain $z(x, y)$ for each pixel (x, y) .

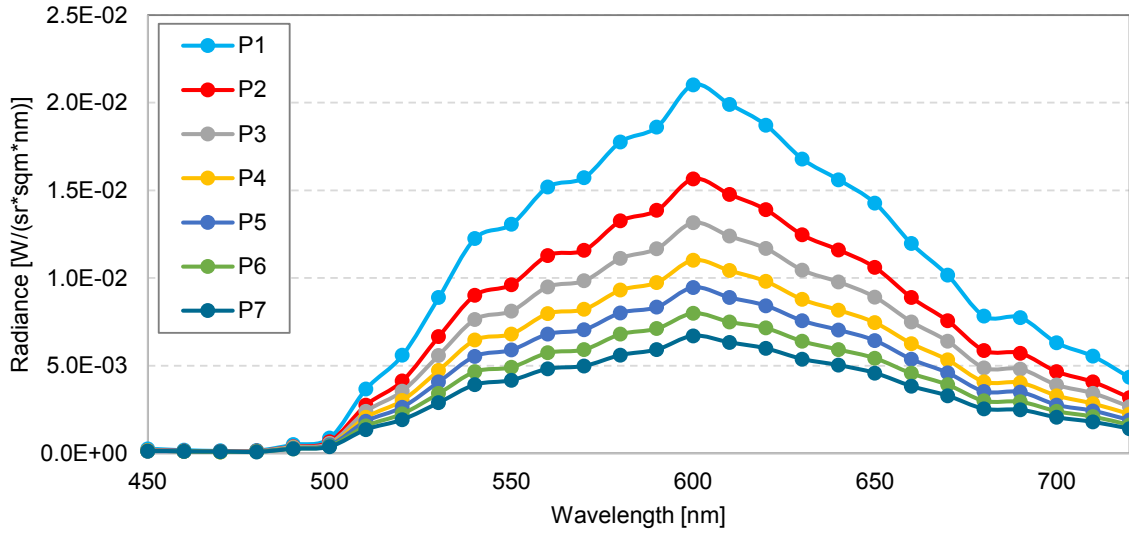
$$\mathbf{M} \begin{bmatrix} z_1(x, y) \\ z_2(x, y) \\ \vdots \\ z_N(x, y) \end{bmatrix} = \begin{bmatrix} N_{x,1}/N_{z,1} \\ N_{y,1}/N_{z,1} \\ N_{x,2}/N_{z,2} \\ N_{y,2}/N_{z,2} \\ \vdots \\ N_{x,n}/N_{z,n} \\ N_{y,n}/N_{z,n} \end{bmatrix}, \quad (4.6)$$

where n is the number of pixels to calculate and \mathbf{M} is a $2n$ by n sparse matrix of which at most two entities are non-zeros (1 or -1) for each column. Solving Eq. (4.6) yields a set of $\{x, y, z\}$ for every pixel of the object. We save the 3D geometry in a Wavefront OBJ file. Adjacent vertices are connected through edges so that every three vertices form a face in the 3D model. We connect the vertices in a way that all the faces of the 3D model face toward the front direction.

(a) Measurement setup & captured image



(b) Spectral measurement of interreflection



(c) Reconstructed geometry

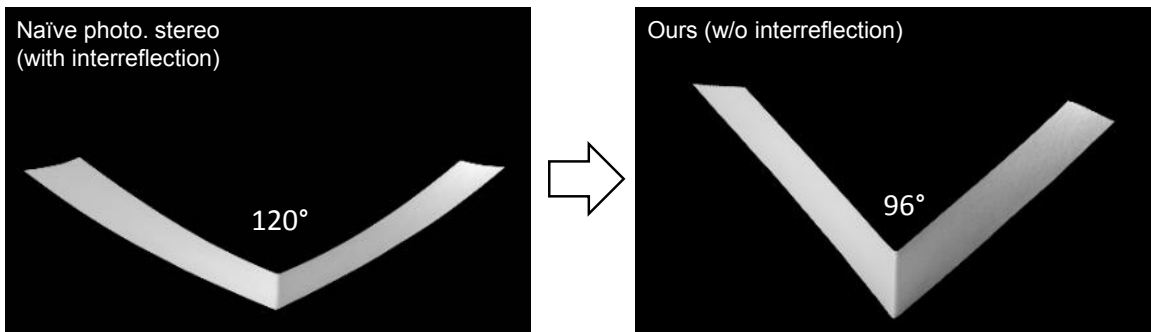
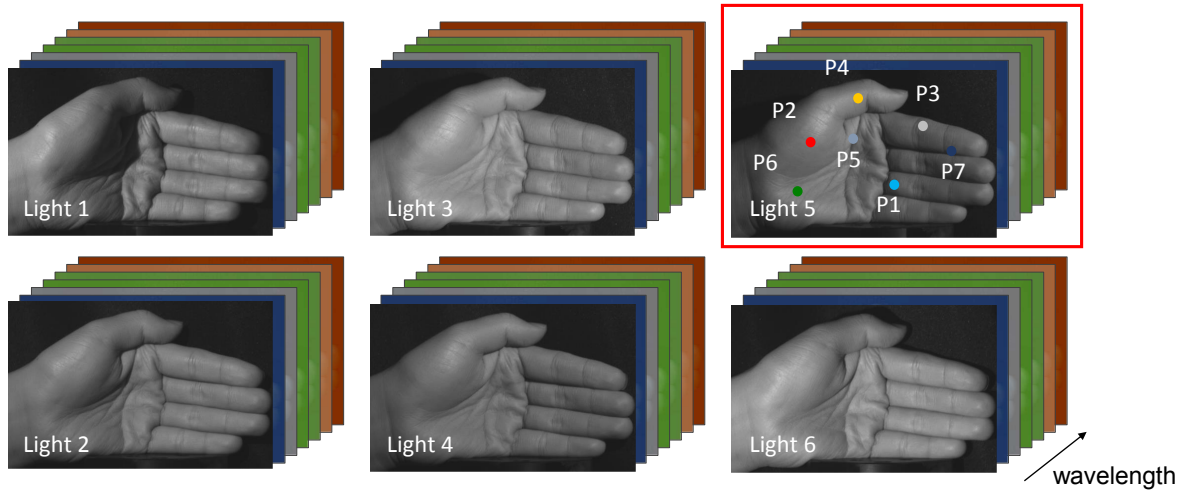
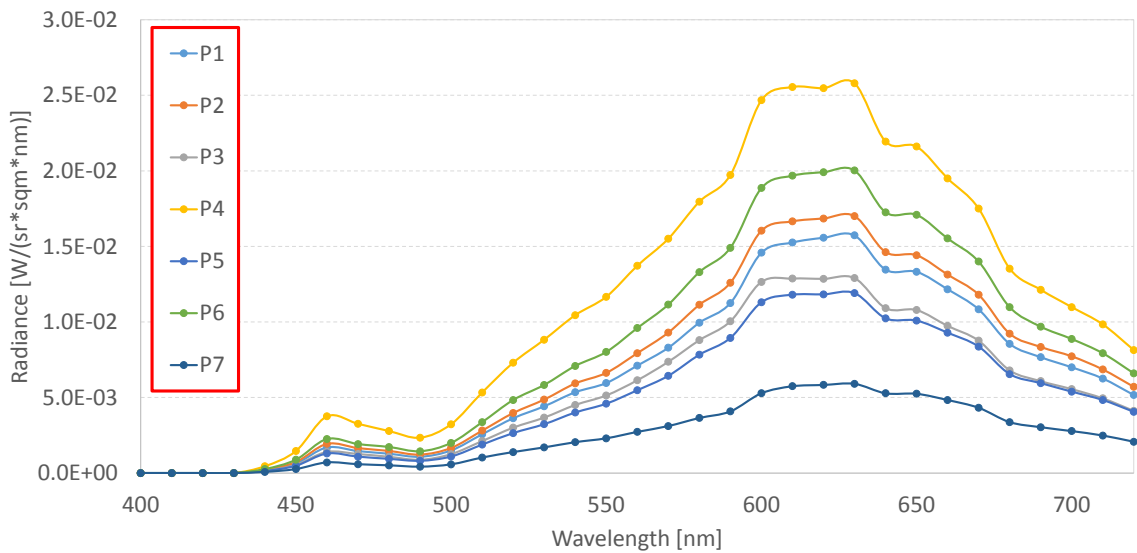


Figure 4.6: Schematic diagram of our multispectral photometric stereo that removes interreflection effectively. (a) shows the measurement setup and captured image of the target object (L-shaped in 90°). The inner faces of the object present interreflection along with direct reflection. (b) presents the radiometric power distribution (captured by a multispectral camera) over the seven points on the left-hand-side surface with interreflection. (c) compares the reconstructed 3D geometries using ordinary photometric stereo with interreflection and our method that removes interreflection using multispectral photometric stereo.

(a) Multispectral images per light source



(b) Spectral measurement of interreflection



(c) Normal map



(d) Reconstructed geometry



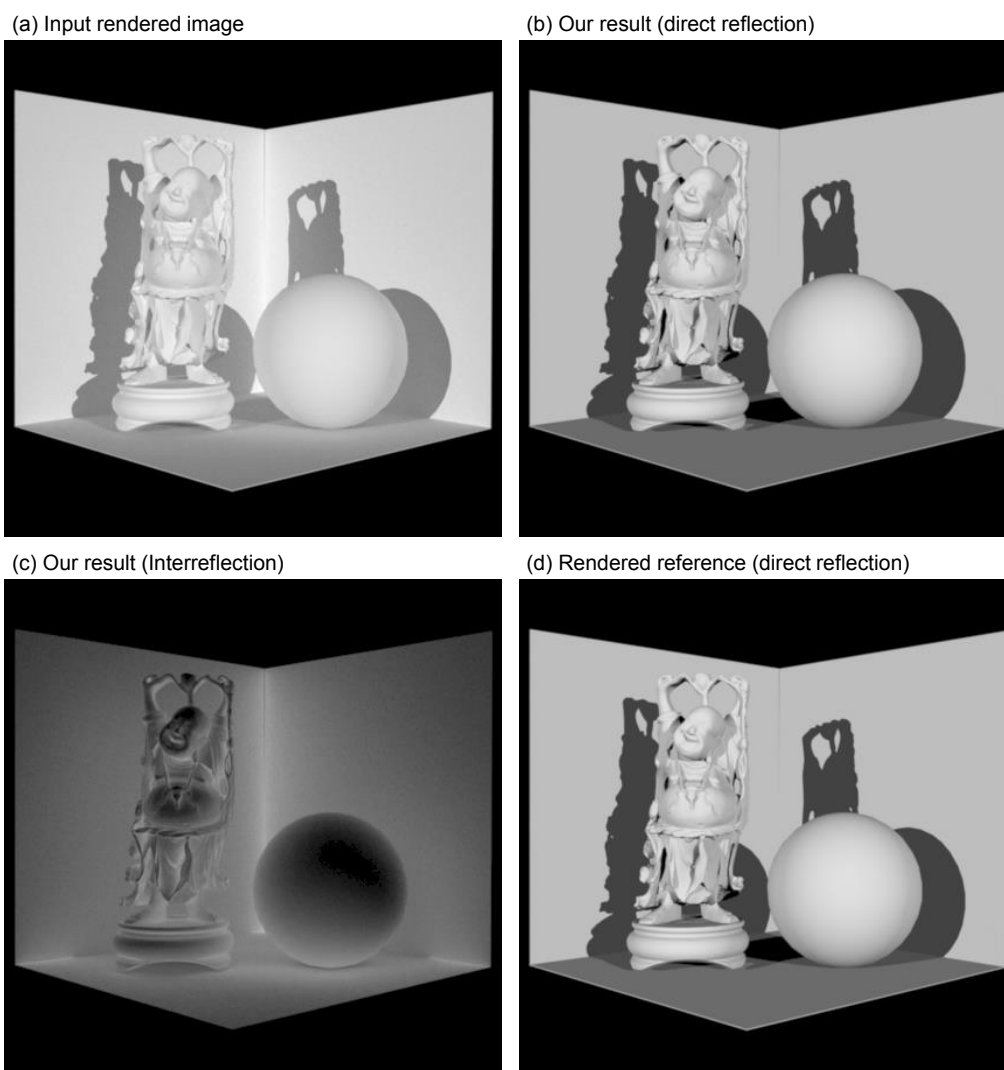
Figure 4.7: An example of acquiring the 3D shape of a real-world object (a hand). (a) shows six multispectral images under each light source. (b) demonstrates the spectral power distributions of seven points on the hand as examples. We remove interreflection using the spectral information of each point. (c) is a estimated surface normal map as an output of our method. (d) shows a reconstructed 3D shape from the normal map. By removing interreflection, we enhance the accuracy of the normals and geometry. Camera settings: Shutter speed: 80 ms, Gain: 0 dB, F/stop: 2, F-length: 35 mm

Chapter 5. Results

In order to recover a 3D shape, our multispectral photometric stereo system captures six multispectral images of 29 channels, from 440 nm to 720 nm in 10 nm intervals, with the LED lights at different positions (see Fig. 4.3). We then perform the proposed multispectral interreflection removal method and conduct photometric stereo with the images exclusively under direct illumination.

5.1 Separating Direct and Indirect Illumination

We evaluate our multispectral interreflection algorithm with ground truth data generated by a multispectral rendering technique. Mitsuba renderer [13] is used to simulate our multispectral imaging. We render a multispectral image with a similar setting to our multispectral photometric stereo system: 33 channels from 400 nm to 720 nm with 10 nm intervals. Fig. 5.1 and Fig. 5.2 present the results of our simulation: Happy Buddha with a sphere and Max Planck with an octahedron. For both figures, we perform our interreflection removal method with a fourth-bounded light model, i.e., we separate up to the fourth-bounded lights from the direct reflection. Both scenes are lit under two directional lights of which the spectral power distribution is same as that of an LED light. The multispectral reflectance of the object is manually set as an orange color. (a) shows the input rendered image at 600 nm channel, i.e., the brightest channel, with interreflection. The concave areas of the object and the corner between the two walls are brighter than the neighboring areas due to the interreflection. (b) presents the result of our multispectral interreflection removal method, i.e., the direct reflection image. (c) shows the interreflection effect of the scene, which is the sum of the second, the third and the fourth-bounded lights. (d) shows the reference image of direct reflection. For the reference image, we set the maximum bounce value of the path tracer as two. In (e), we plot the peak signal-to-noise ratio (PSNR) between our result (b) and the reference (d). Our method yields an accurate result even with the second-bounded model ($\approx 26\text{dB}$) and yields an undistinguishable result with the third-bounded model ($\approx 35\text{dB}$). The PSNR increases as we raise the number of bounce from two to four and begins to saturate from the fourth-bounded light model.



(e) PSNR between (b) and (d)

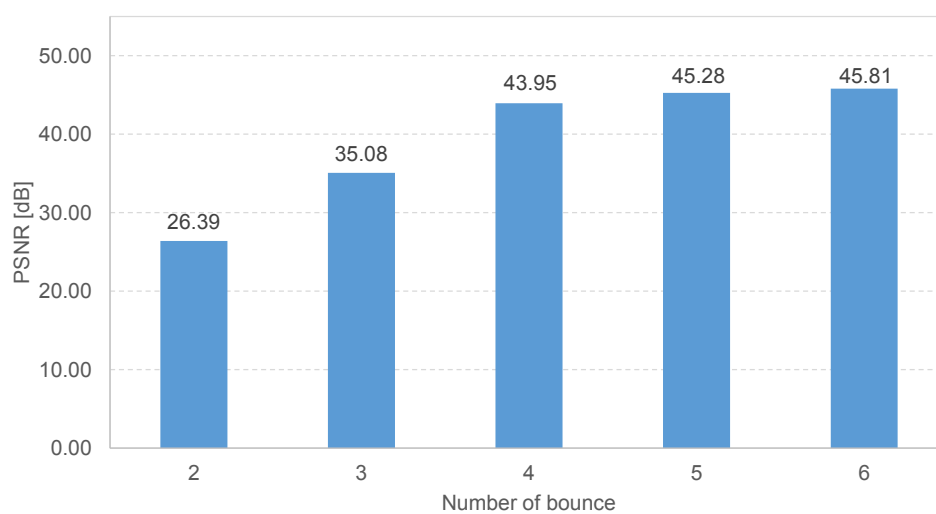
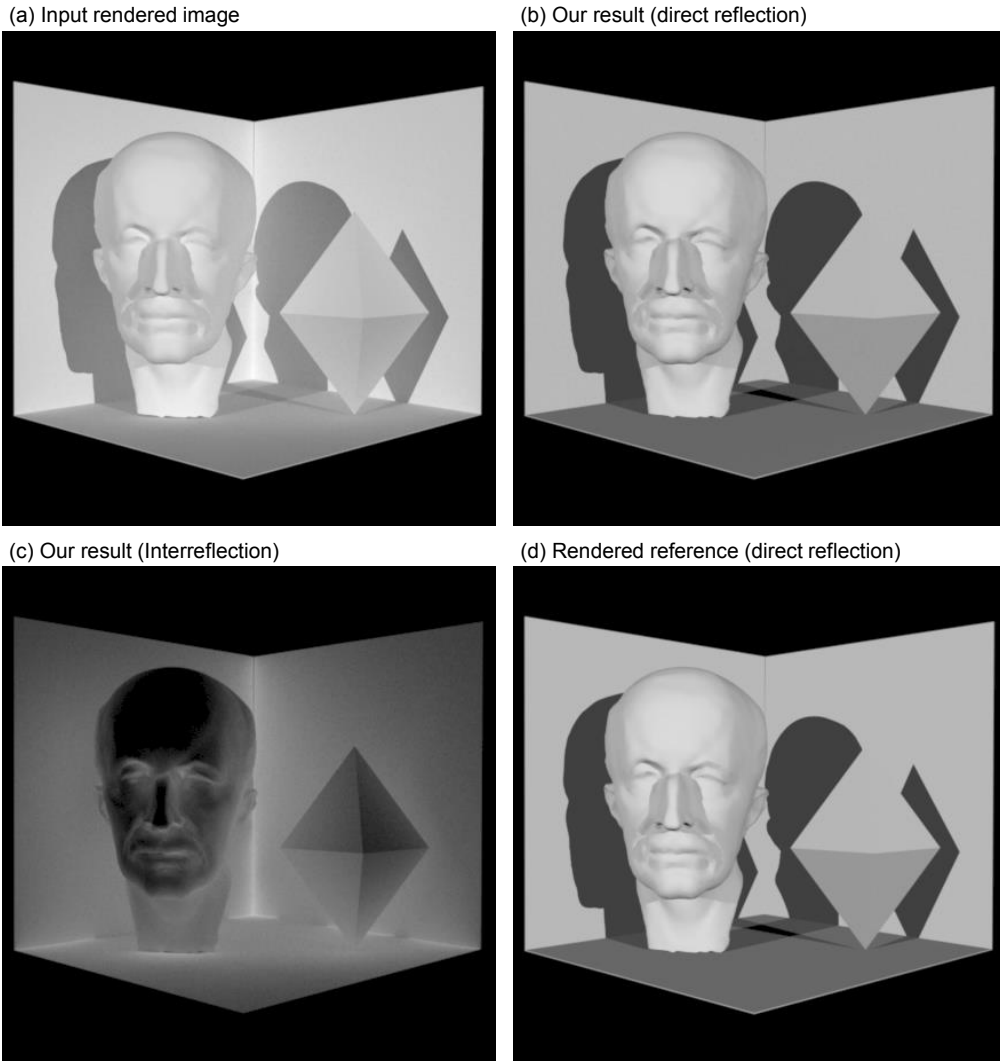


Figure 5.1: *Direct/indirect illumination separation with multispectral rendering with Mitsuba renderer. (a) shows the input rendered image at 600 nm channel. (b) presents the direct reflection image as a result of our method with fourth-bounded model. (c) shows the interreflection effect, the sum of second, third and fourth-bounded lights. (d) shows the rendered reference of direct reflection. peak signal-to-noise ratio (PSNR) between (b) and (d) are shown in (e). The PSNR increases as we raise the number of bounce from two to four and begins to saturate from the fourth-bounded light model.*



(e) PSNR between (b) and (d)

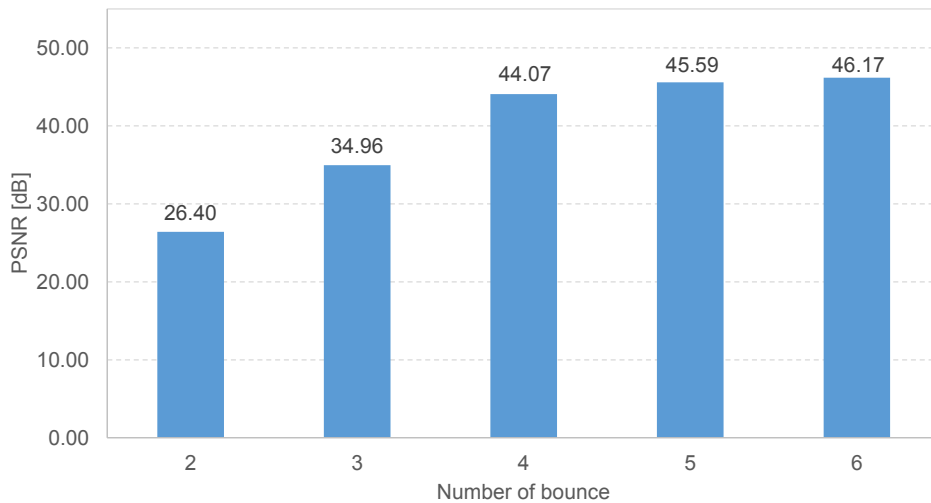


Figure 5.2: Direct/indirect illumination separation with multispectral rendering with Mitsuba renderer. (a) shows the input rendered image at 600 nm channel. (b) presents the direct reflection image as a result of our method with fourth-bounded model. (c) shows the interreflection effect, the sum of second, third and fourth-bounded lights. (d) shows the rendered reference of direct reflection. peak signal-to-noise ratio (PSNR) between (b) and (d) are shown in (e). The PSNR increases as we raise the number of bounce from two to four and begins to saturate from the fourth-bounded light model.

5.2 Accuracy in Acquiring a 3D Shape

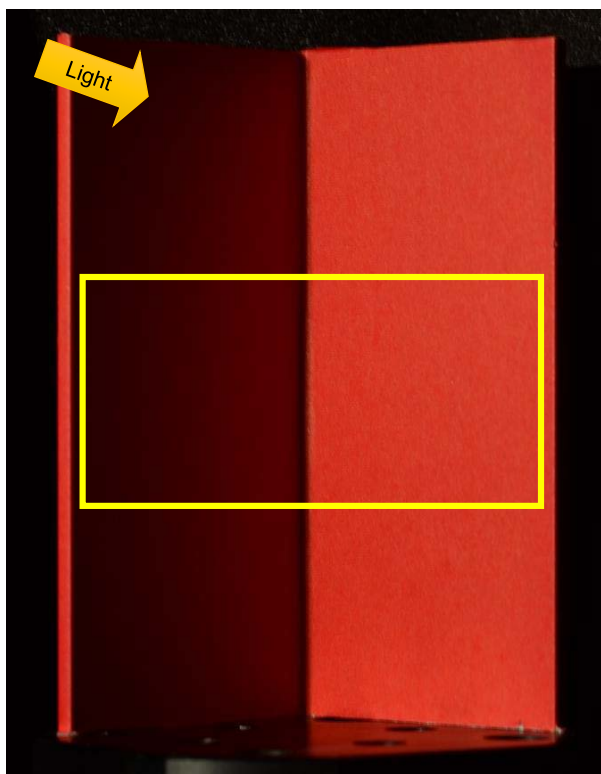
We evaluate the accuracy of our system, using an L-shaped object with a diffuse color. An L-shaped object is useful in evaluating normal estimation and 3D reconstruction as its geometry is known as 90° of internal angle between two faces.

Fig. 5.3 illustrates an example of separating direct and indirect illumination from interreflection using our method. We quantitatively evaluate the accuracy of acquiring a 3D shape (a) with known geometry (90° -angled). (b) shows the illumination separation results. As the light illuminates the L-shaped object from the left side, the interreflection dominantly occurs on the left-sided face of the object. (c) compares the reconstructed shapes from the normals with a naïve photometric stereo (with interreflection) and our multispectral photometric stereo method (without interreflection). The reconstructed shape with interreflection shows a less concave shape than the shape without interreflection. The reconstructed shape without interreflection has a flat surface, a sharp edge, and an accurate internal angle.

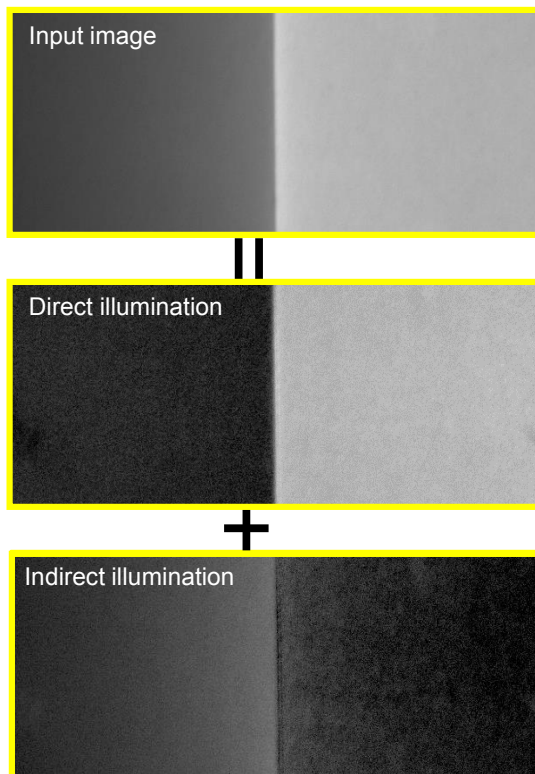
Fig. 5.4 compares the reconstructed internal angle between the two faces of the L-shaped object. The internal angle was calculated by averaging the angles between two normal vectors on each symmetric side of the L-shaped object. Fig. 5.4 (a) compares the performance of an active photometric stereo method with a beam projector [19], our method using an RGB camera, and our method using the multispectral camera. For the comparison, we calibrate an ordinary RGB camera (Point Grey FL3-GE-13S2C-C) radiometrically and apply our proposed method for this trichromatic input. Fig. 5.4 (a) shows that our method using the multispectral imager yields a highly accurate internal angle (91.59°) with smaller standard deviation ($\sigma=6.51^\circ$) than the active method [19] (96.01° , $\sigma=18.35^\circ$) or the RGB camera (97.65° , $\sigma=14.95^\circ$). As we calculate the internal angle pixel-by-pixel, larger deviation implies larger noise, i.e., our multispectral method performs better than the others. We could trace back this result caused by the wide spectral bandwidth of the trichromatic camera (roughly 100 nm–200 nm per channel). Using wide sensing bandwidth suffers from losing the spectral details of wavelength-dependent reflectance as metamerism.

Fig. 5.4 (b) shows the experimental results with different surface colors. We evaluate our multispectral method with the L-shaped structure with four colors: red, green, blue and yellow. When interreflection was removed, the internal angle improved by 16.75% on average for the four test colors. This indicates that our multispectral interreflection removal method works well regardless of the surface color of the object. Tables 5.1 and 5.2 show the internal angles and their standard deviations with various experimental settings.

(a) An L-shaped object (90-degree)



(b) Separating interreflection



(c) Normal map & reconstructed geometry

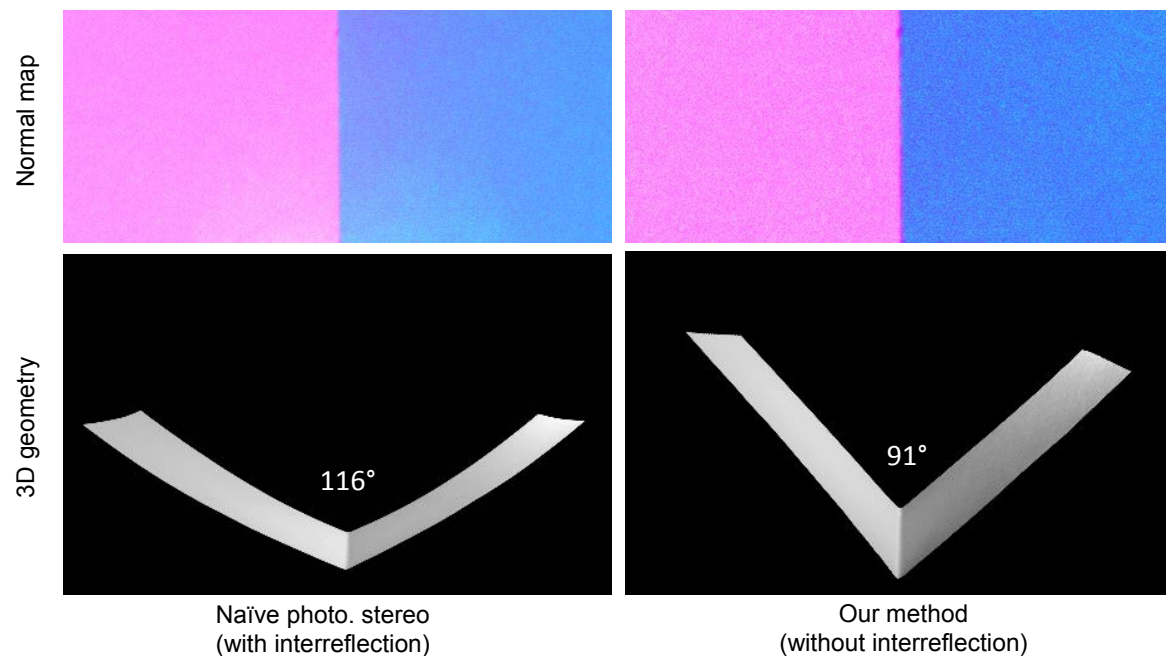


Figure 5.3: Evaluating the effect of our interreflection removal method and the geometric accuracy of the estimated surface. (a) shows an L-shaped metal object, of which the angle was fabricated to have a measure of 90° . This metal object is covered by a red paper to make it a diffuse surface. (b) describes the separation of direct and indirect illumination using our method. The illustrated image shows the light energy at the wavelength of 630 nm. (c) compares the reconstructed geometries with and without interreflection. Our proposed method significantly improves the accuracy in measuring a 3D shape with photometric stereo. Camera settings: shutter speed: 70 ms, gain: 0 dB, f/stop: 2, f-length: 35 mm

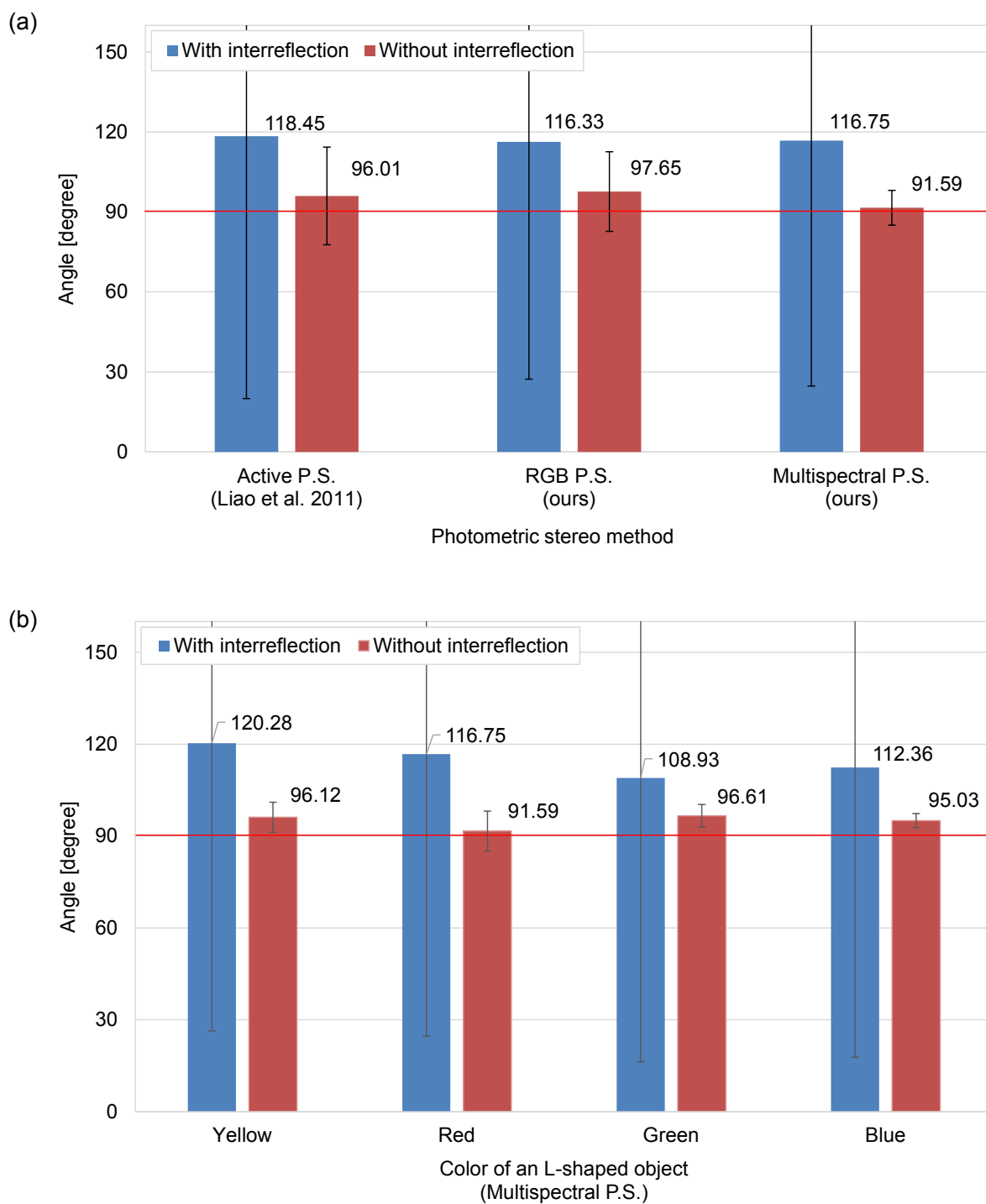


Figure 5.4: Quantitative comparison of the reconstructed angles (physical angle measure: 90°). (a) is reconstructed using an projector-based active photometric stereo method [19]. (b) is the result of our method using an ordinary RGB camera. (c) shows the result angle using our multispectral method. Our multispectral method improves the reconstruction accuracy significantly and consistently.

	Active P.S. (Liao et al. 2011)		RGB P.S. (ours)		Multispectral P.S. (ours)	
	Mean	Std	Mean	Std	Mean	Std
With interreflection	118.45°	98.48°	116.33°	89.07°	116.75°	92.1°
Without interreflection	96.01°	18.35°	97.65°	14.95°	91.59°	6.51°

Table 5.1: *Inter-comparison using an L-shaped object. We compare the performance of three methods: an active photometric stereo method with a beam projector [19], our method using an RGB camera, and our method using the multispectral camera. We calculated the internal angle between the two faces of the L-shaped object. Our method using the multispectral imager yields a highly accurate internal angle with smaller deviation than the others.*

	Multispectral Photometric Stereo							
	Yellow		Red		Green		Blue	
	Mean	Std	Mean	Std	Mean	Std	Mean	Std
With interreflection	120.28°	93.89°	116.75°	92.1°	108.93°	92.61°	112.36°	94.61°
Without interreflection	96.12°	4.94°	91.59°	6.51°	96.61°	3.68°	95.03°	2.32°

Table 5.2: *Intra-comparison using an L-shaped object. We evaluate our multispectral method with L-shaped structure with 4 colors: red, green, blue and yellow. We calculated the internal angle between the two faces of the L-shaped object. The internal angle improved by 16.75% on average for the four test colors. This indicates that our multispectral interreflection removal method works well regardless of the surface color of the object.*

5.3 Scanning 3D Objects

This section demonstrates 3D scanning applications with several 3D objects.

Fig. 5.5 shows the experimental results of our multispectral photometric stereo with an orange. When scanning an object with a grainy texture, such as an orange, it is technically demanding to preserve the high frequency geometrical details. (a) shows the normal map and reconstructed 3D geometry using naïve photometric stereo which suffer from interreflection. The normal map is somewhat blurred and the 3D geometry is lack of the grainy texture of the orange. (b) presents the results of our method. The high frequency geometrical details are well presented both on the normal map and in the 3D geometry.

Fig. 5.6 presents surface normal maps of a plaster figure of Mars, painted with a diffuse red color. We qualitatively compare the surface normal maps, estimated by naïve photometric stereo (b), Liao et al. [19] (c) and our method (d). (b) shows the normal map estimated with interreflection. High frequency details of surface gradients are integrated into the interreflection effect. The estimated normal map therefore appears blurred. (c) is the normal map estimated by the active photometric stereo method [19]. While high frequency details are recovered, the normal map suffers from severe noise. (d) shows the normal map by our method using multispectral photometric stereo system. Removing interreflection by our multispectral method reveals the high frequency details of the surface normals without struggling with the noise.

Fig. 4.7 presents an example of 3D scanning of a real-world object, a hand. (a) shows the multispectral

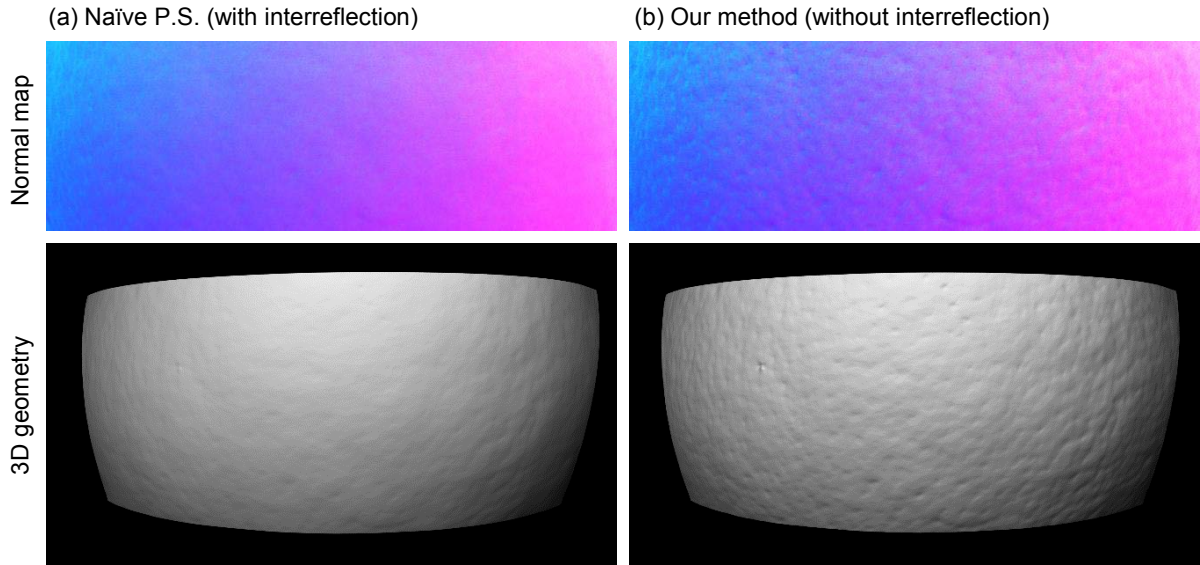


Figure 5.5: Normal maps and reconstructed 3D geometries of an orange before and after interreflection removal. (a) shows results using naïve photometric stereo which suffer from interreflection. The normal map is somewhat blurred and the 3D geometry is lack of the grainy texture of the orange. (b) presents the results of our method. The high frequency geometrical details are well presented both on the normal map and in the 3D geometry. Camera settings: shutter speed: 80 ms, gain: 0 dB, f/stop: 2, f-length: 35 mm

images under six different light sources. (b) presents the spectral measurement of reflection in the case of a bent hand. For seven selected points from $P1$ to $P7$, we plot the spectral power distribution (SPD) functions over the scanned bandwidth. These different points show the different shapes of SPDs because the portion between the direct illumination and the indirect illumination on each point varies. The shape of SPD is determined by how much light energy is contributed from the indirect illumination. (c) demonstrates the output of a normal map and (d) is a 3D model obtained by our multispectral photometric stereo method. In (c) and (d), we can see the high frequency details, i.e., the wrinkles, are well recovered in a bent area.

We estimate a normal map and reconstruct the geometry of a plaster figure of David. Fig. 5.7 compares the normal map and the 3D geometry model reconstructed by (a) a 3D scanner, NextEngine, (b) Liao et al. [19], and (c) our multispectral photometric stereo. The curly hair of the figure makes it difficult to estimate accurate surface normals due to the interreflection. As the 3D scanner utilizes the triangulation method to reconstruct the geometry, its output is considered as a ground truth geometry even though it struggles with occlusion around the concave faces. Our multispectral photometric stereo system yields accurate surface normals and provides geometrical details as much as the ground truth.

Fig. 5.8 compares the performance variation of our method according to the number of input spectral channels. We scan a concave-shaped soap, which can maximize the interreflection. As the soap has specular reflection, we use polarizing filters to prevent the specular reflection comes into the sensor directly. The LCTF has its own linear polarizing filter in its optical path. We attach additional linear

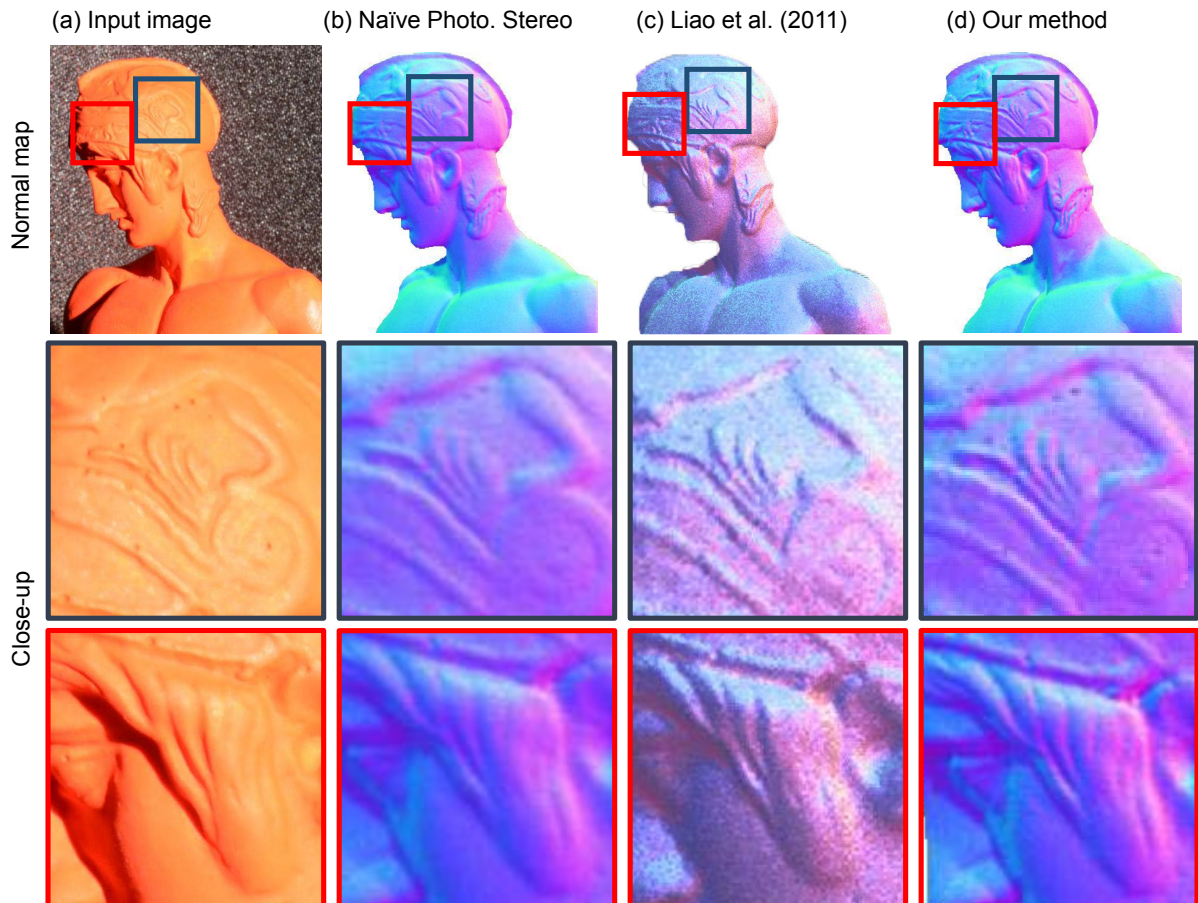


Figure 5.6: Normal estimation with interreflection removal. (a) is a photograph of the scene. The scanned object is a plaster figure of Mars. (b) shows an estimated surface normals with interreflection. The geometrical details are lost due to the interreflection. (c) presents the surface normal map estimated using active method [19]. Although the geometrical details are revealed, the surface normal map also includes noise. (d) shows the output surface normal map of our method using multispectral imager. High frequency details remain while yielding a clean normal map. Camera settings: shutter speed: 70 ms, gain: 0 dB, f/stop: 2, f-length: 35 mm

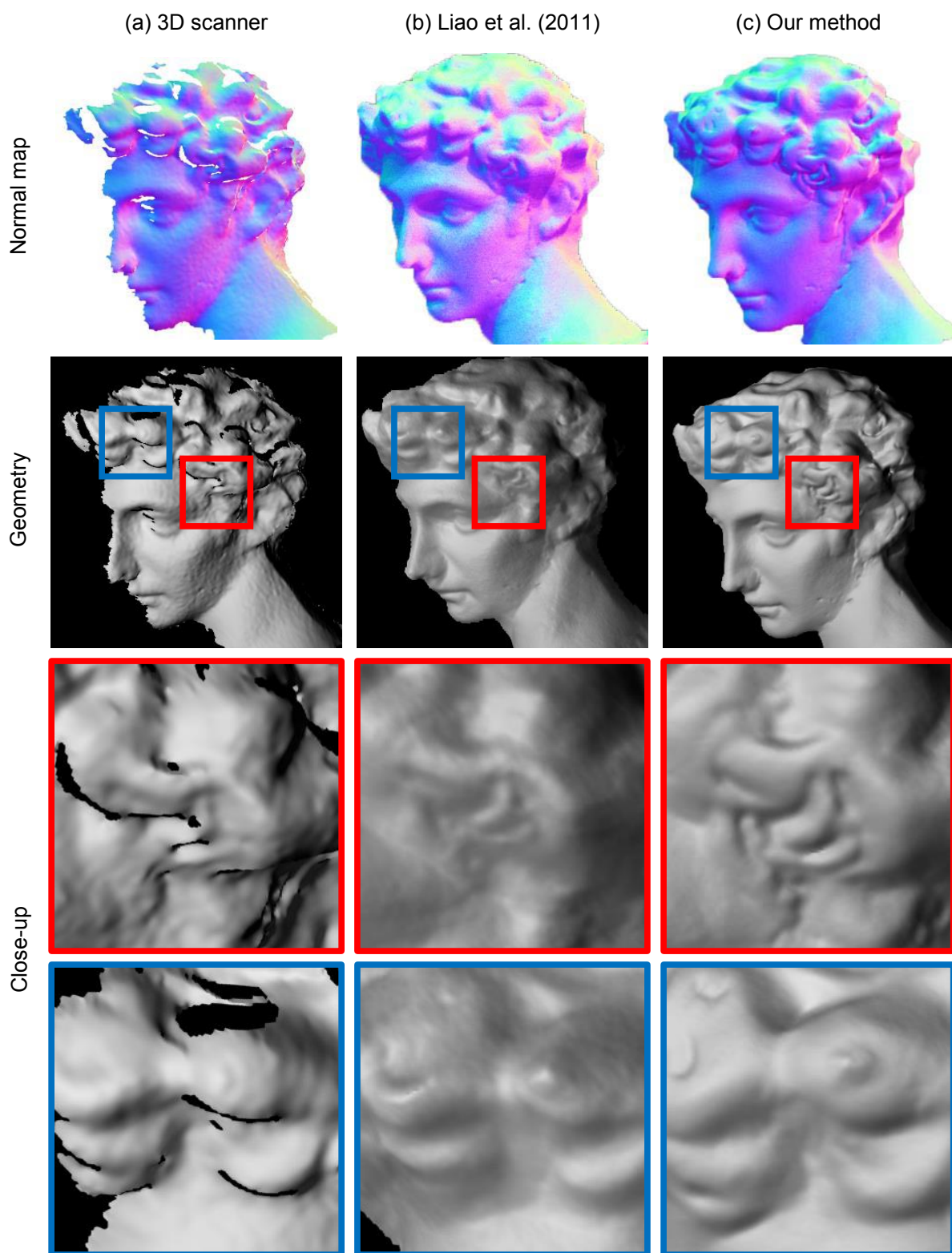


Figure 5.7: Comparison among the results of (a) a 3D scanner (reference), (b) projector-based photometric stereo [19], and (c) our multispectral photometric stereo. Our method yields better surface normals and the 3D model compared to the active method. The 3D model reconstructed by our method includes details as much as the reference. Camera settings: shutter speed: 70 ms, gain: 0 dB, f/stop: 2, f-length: 35 mm

polarizing filters in front of the light sources in a way that the linear direction of the filters are orthogonal to that of the LCTF. (a) shows the ground truth obtained by a 3D laser scanner (NextEngine). (b) shows the reconstruction results of the normals and 3D geometry with the naïve photometric stereo approach (without removing interreflection). The reconstructed geometry is flattened compared to the ground truth. (c) and (d) present the normals and 3D models using our method with two different imagers: an RGB camera and our multispectral imager. In (c), although the reconstructed geometry is still somewhat flattened, there is an improvement in terms of sharpness on the edges. (d) shows the results of our multispectral photometric stereo system using 29 channels. Compared to the ground truth, our method yields virtually identical geometry to the ground truth. Using a sufficient number of channels, our method can acquire high-frequency details of the object surface, yielding high-fidelity surface normals and 3D models.

Fig. 5.9 and Fig. 5.10 show the experimental results of a human face. Facial features, such as a nose, a mouth and eyes, makes the overall shape of the face a mixture of concave and convex areas. In particular, the area between two eyes, the area between a nose and a cheek and the area between two lips are vulnerable to the interreflection. In addition, the rough skin also produces the interreflection in a micro scale. (a) and (b) show the results of the naïve photometric stereo and those of our multispectral photometric stereo. The reconstructed geometry in (a) shows a flattened facial shape and a smooth skin. In contrast, in (b), the concavity, as well as the convexity, of the face are well preserved and the skin keeps the roughness of the human skin. (c) and (d) show the close-ups of (a) and (b), respectively. Note that, tiny features in the skin, such as acne, are blurred in (c) and only recovered by our method in (d).

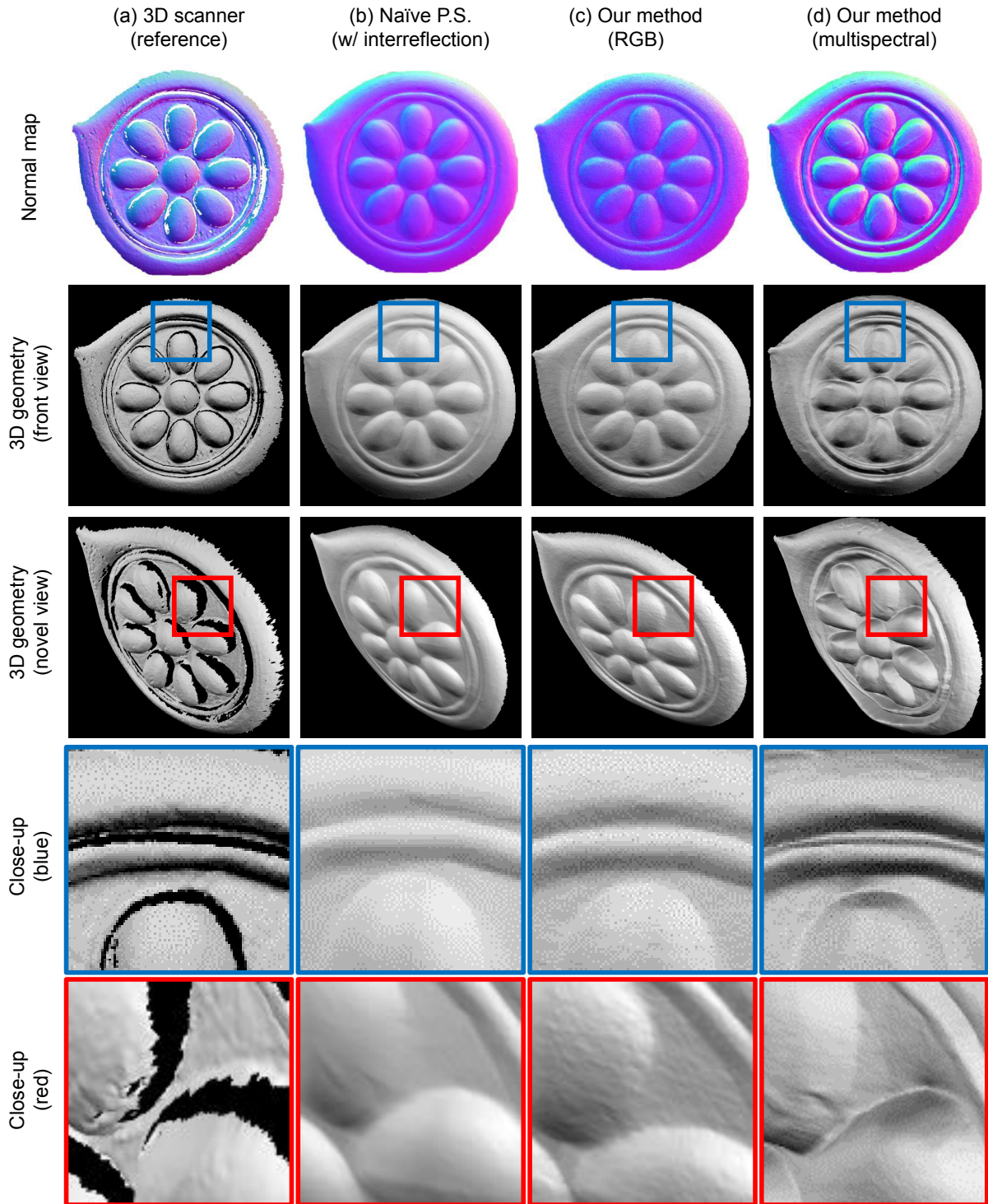


Figure 5.8: The comparison of the reconstructed 3D models depending on the number of input spectral channels. (a) shows the ground truth obtained by a 3D laser scanner (NextEngine). (b) shows results of a naïve photometric stereo without removing interreflection. The surface is flatten compared to the ground truth. (c) presents applying our multispectral method to an RGB camera using three spectral channels. There is a small improvement compared to the naïve approach, in terms of sharpness on the edges. (d) presents the results of our multispectral photometric stereo using 29 channels. The reconstructed geometry is virtually identical to the ground truth. Camera settings: shutter speed: 200 ms, gain: 0 dB, f/stop: 2, f-length: 35 mm

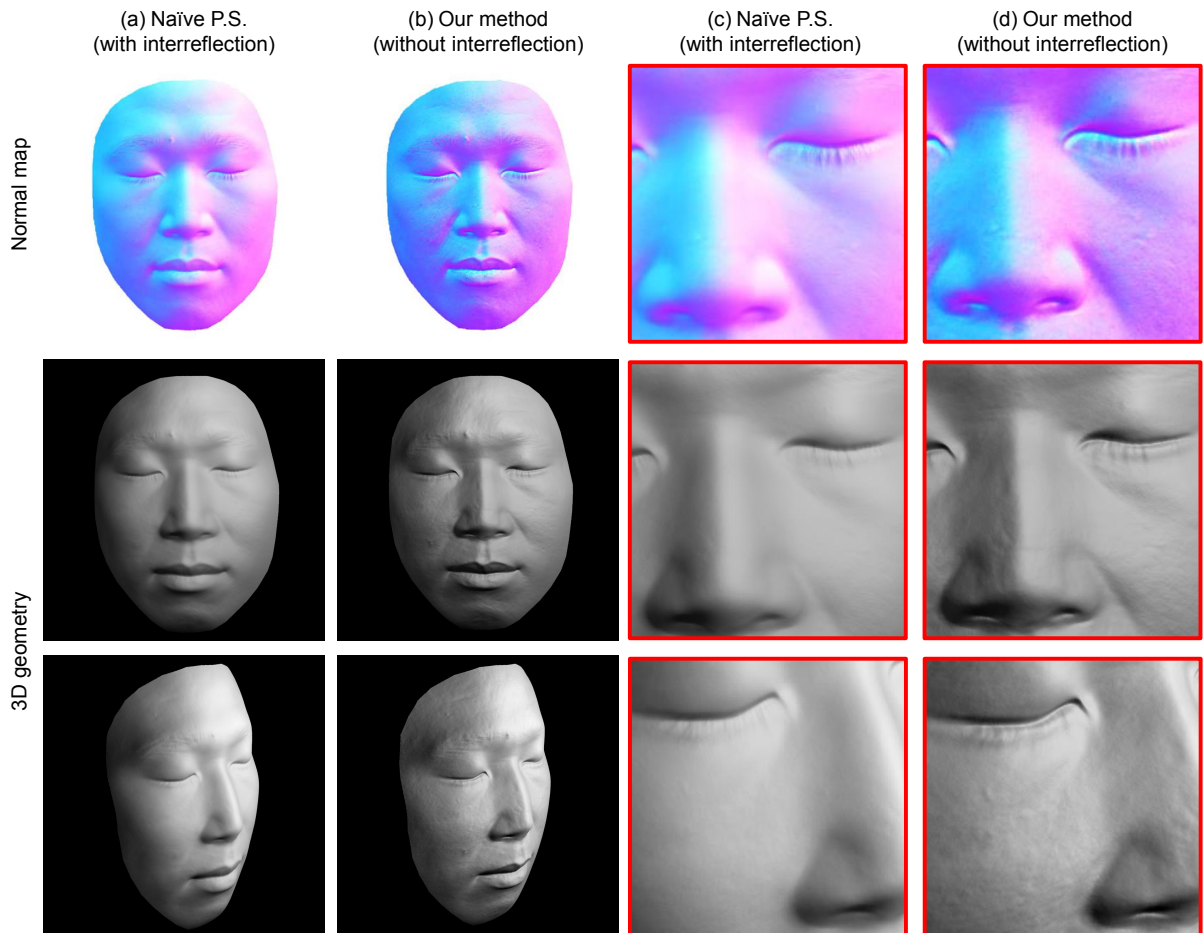


Figure 5.9: *The experimental results of scanning a human face (#1). (a) shows the normal map and the reconstructed 3D geometry using naïve photometric stereo. (b) shows the results from our multispectral photometric stereo. (b) presents the concavity and the convexity of the facial features better than (a). In addition, the roughness of the human skin is well recovered in (b). (c) and (d) show the close-ups of (a) and (b), respectively. Note that, tiny features in the skin, e.g., acne, are only recovered by our method in (d). Camera settings: shutter speed: 20 ms, gain: 0 dB, f/stop: 2.8, f-length: 24 mm*

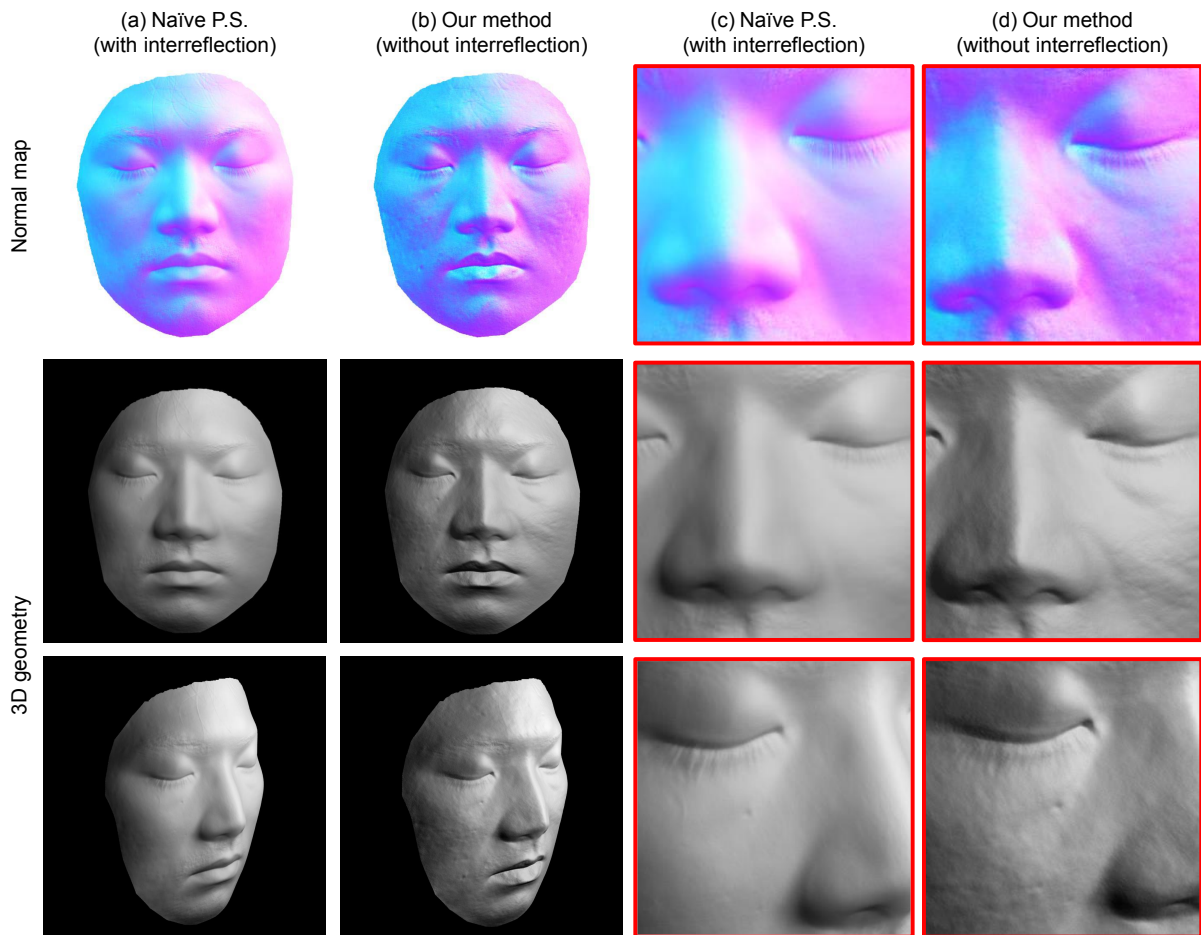


Figure 5.10: *The experimental results of scanning a human face (#1). (a) shows the normal map and the reconstructed 3D geometry using naïve photometric stereo. (b) shows the results from our multispectral photometric stereo. (b) presents the concavity and the convexity of the facial features better than (a). In addition, the roughness of the human skin is well recovered in (b). (c) and (d) show the close-ups of (a) and (b), respectively. Note that, tiny features in the skin, e.g., acne, are only recovered by our method in (d). Camera settings: shutter speed: 20 ms, gain: 0 dB, f/stop: 2.8, f-length: 24 mm*

Chapter 6. Discussion and Future Work

In this thesis, we proposed a multispectral photometric stereo system for estimating the accurate surface normals by removing interreflection over monochromatic diffuse surfaces. Our method allows us to reconstruct 3D geometry models with a high accuracy. One of the virtues of our system is that the multispectral and 3D geometry information are well aligned as the geometric information is derived from the multispectral information directly. The multispectral imaging enables the physically-meaningful acquisition of a scene, which is unsatisfactory in case of the trichromatic images. In addition, our method does not assume or require a specially designed illumination, e.g., structured light patterns or spectral light controls, and thus can be applied in any existing photometric stereo systems by adding a multispectral camera.

As our multispectral interreflection removal method is a per-pixel operation, the camera sensor noise may degrade the performance of our algorithm. We overcame the problem by using enough number of channels, 29 channels. As the sensor noise has gaussian distribution, multiple sampling may cancel out the noise. Theoretically, the more we sample, the more robust our algorithm is. However, we could not explain the quantitative correlation between the number of channels and the accuracy of our method in this work. This is a complicated issue because determining the number of channels is related to sampling multispectral wavelength, and the multispectral wavelength is related to the reflectance of the surface. The quantitative correlation between the optimal sampling of multispectral wavelength and the reflectance of the object is yet unknown. We leave this as our future work.

Our method employs the wavelength-dependent reflectance to figure out how much light energy is from direct and indirect illumination. Therefore, this method might not perform well in the case of gray-scale object. In addition, the monochromatic constraint limits our work and makes it difficult to handle the color blending. In future work, we are going to take into account the color bleeding effect in our model. By using the spectral information of n -bounded lights, we expect to separate the color bleeding effect using iterative method.

Our multispectral imager differentiates the spectral power information using an LCTF. Thus, the acquisition of the spectral information of the objects are limited to static ones due to the electrical transmittance changes of the LCTF along the target wavelength. We are planning to handle this problem using brighter light sources so that each acquisition time (shutter speed) in multispectral channel becomes shorter. Another way to overcome the limitation is to utilize the dispersion based multispectral camera. However, we are not sure yet if the dispersion based multispectral camera yields high resolution images

which are enough for our purpose.

We believe that removing interreflection is not the only benefit of using the multispectral imaging. Besides the interreflection, there exist several assumptions in photometric stereo: no specular reflections, no shadows, calibrated light sources, etc. In our future work, we expect to lift some of these assumptions using multispectral reflectance analysis. In addition, we are considering adding infra-red or ultra-violet light sources in the capture process. This would allow us to capture additional physical reflectance properties of an object, e.g., fluorescence.

Although our method has some limitations mentioned above, our method has its advantage on yielding accurate results on arbitrary shapes. Most of the real world objects are mixtures of concave and convex areas. As traditional photometric stereo algorithms assume the scanned object to be a convex one, they are not suitable for the real world applications. Therefore, we expect that our method would be useful in the real world applications of estimating surface normals and 3D shapes, e.g., industrial defect inspection, digital conservation of cultural heritage, and facial scanning for the entertainment and movie industry.

Chapter 7. Conclusion

We present a novel multispectral photometric stereo method that allows us to remove indirect illumination from reflection and to reconstruct high-fidelity surface normals and geometry exclusively from direct illumination to a high accuracy. We validate the performance of our method, compared with other projector-based approaches in terms of 3D geometry. In contrast to other projector-based approaches, our method could be easily integrated to the existing photometric stereo systems by simply substituting the RGB camera with a multispectral camera. We have demonstrated its usefulness for high-fidelity geometric acquisition in forms of surface normals and 3D models.

Appendices

Appendix A. Calibration Data

A.1 X-rite Mini ColorChecker

A.1.1 Spectroradiometer

Colorchecker radiance #1 - #12 [W/(sr*sqm*nm)]												
Wave-length	#1	#2	#3	#4	#5	#6	#7	#8	#9	#10	#11	#12
440	0.0003	0.0008	0.0013	0.0002	0.0017	0.0015	0.0003	0.0017	0.0006	0.0006	0.0004	0.0003
450	0.0008	0.0025	0.0039	0.0007	0.0051	0.0046	0.0007	0.0051	0.0017	0.0017	0.0011	0.0009
460	0.0008	0.0028	0.0039	0.0008	0.0051	0.0052	0.0008	0.0051	0.0017	0.0016	0.0012	0.0010
470	0.0006	0.0024	0.0030	0.0007	0.0039	0.0045	0.0007	0.0037	0.0013	0.0011	0.0011	0.0009
480	0.0005	0.0022	0.0022	0.0006	0.0028	0.0038	0.0007	0.0025	0.0010	0.0008	0.0010	0.0008
490	0.0007	0.0032	0.0027	0.0009	0.0033	0.0053	0.0009	0.0026	0.0012	0.0008	0.0018	0.0011
500	0.0010	0.0050	0.0036	0.0014	0.0044	0.0080	0.0013	0.0030	0.0016	0.0011	0.0038	0.0016
510	0.0014	0.0069	0.0047	0.0022	0.0055	0.0111	0.0021	0.0034	0.0022	0.0013	0.0075	0.0026
520	0.0020	0.0081	0.0057	0.0036	0.0064	0.0144	0.0034	0.0037	0.0027	0.0015	0.0126	0.0049
530	0.0025	0.0083	0.0063	0.0054	0.0071	0.0167	0.0052	0.0038	0.0031	0.0016	0.0171	0.0093
540	0.0028	0.0086	0.0066	0.0062	0.0076	0.0176	0.0066	0.0038	0.0035	0.0017	0.0197	0.0139
550	0.0032	0.0097	0.0068	0.0063	0.0080	0.0178	0.0080	0.0038	0.0038	0.0019	0.0212	0.0172
560	0.0039	0.0111	0.0073	0.0065	0.0085	0.0189	0.0111	0.0040	0.0046	0.0022	0.0238	0.0213
570	0.0048	0.0124	0.0072	0.0062	0.0085	0.0181	0.0156	0.0041	0.0055	0.0024	0.0242	0.0245
580	0.0058	0.0156	0.0072	0.0060	0.0089	0.0166	0.0214	0.0042	0.0082	0.0029	0.0234	0.0273
590	0.0069	0.0208	0.0074	0.0060	0.0099	0.0148	0.0281	0.0043	0.0142	0.0037	0.0219	0.0303
600	0.0077	0.0260	0.0077	0.0061	0.0117	0.0134	0.0335	0.0046	0.0223	0.0047	0.0204	0.0334
610	0.0079	0.0286	0.0075	0.0059	0.0126	0.0120	0.0345	0.0047	0.0278	0.0053	0.0184	0.0341
620	0.0076	0.0283	0.0068	0.0056	0.0119	0.0105	0.0323	0.0044	0.0288	0.0053	0.0163	0.0323
630	0.0072	0.0266	0.0060	0.0051	0.0110	0.0091	0.0287	0.0041	0.0270	0.0050	0.0143	0.0292
640	0.0070	0.0253	0.0057	0.0049	0.0110	0.0082	0.0258	0.0040	0.0251	0.0049	0.0128	0.0268
650	0.0064	0.0228	0.0051	0.0044	0.0109	0.0069	0.0220	0.0037	0.0219	0.0045	0.0110	0.0233
660	0.0061	0.0219	0.0049	0.0041	0.0116	0.0063	0.0200	0.0039	0.0200	0.0045	0.0102	0.0213
670	0.0052	0.0195	0.0043	0.0035	0.0109	0.0056	0.0172	0.0038	0.0169	0.0043	0.0091	0.0182
680	0.0042	0.0170	0.0036	0.0028	0.0093	0.0049	0.0147	0.0037	0.0141	0.0041	0.0080	0.0151
690	0.0036	0.0156	0.0031	0.0023	0.0082	0.0046	0.0132	0.0039	0.0123	0.0043	0.0073	0.0133
700	0.0031	0.0140	0.0025	0.0020	0.0071	0.0041	0.0116	0.0041	0.0106	0.0045	0.0065	0.0115
710	0.0026	0.0120	0.0020	0.0016	0.0061	0.0034	0.0098	0.0041	0.0088	0.0044	0.0054	0.0096
720	0.0022	0.0099	0.0017	0.0013	0.0051	0.0027	0.0080	0.0039	0.0071	0.0040	0.0043	0.0078

Table A.1: Spectral measurements of an X-rite Mini ColorChecker (#1 - #12). We first measure the radiance of 24 color patches under static illumination with a spectroradiometer (See Fig. 4.5). And we multiply the transmittance of the LCTF for each channel, yielding the radiance value per wavelength as above. Multiplying the transmittance of the LCTF makes the radiometric calibration robust as it compensates the varying bandwidths of different channels of the LCTF. The numbers in the table correspond to the numbers of the color patches in Fig. 4.5.

Colorchecker radiance #13 - #24 [W/(sr*sqm*nm)]												
Wave-length	#13	#14	#15	#16	#17	#18	#19	#20	#21	#22	#23	#24
440	0.0012	0.0003	0.0002	0.0004	0.0014	0.0014	0.0041	0.0028	0.0016	0.0009	0.0004	0.0002
450	0.0038	0.0010	0.0007	0.0010	0.0040	0.0045	0.0124	0.0083	0.0050	0.0026	0.0013	0.0005
460	0.0040	0.0011	0.0007	0.0011	0.0038	0.0051	0.0129	0.0088	0.0052	0.0028	0.0013	0.0005
470	0.0029	0.0010	0.0006	0.0010	0.0027	0.0043	0.0101	0.0069	0.0041	0.0021	0.0010	0.0004
480	0.0019	0.0010	0.0005	0.0009	0.0019	0.0035	0.0079	0.0053	0.0031	0.0016	0.0008	0.0003
490	0.0018	0.0018	0.0007	0.0015	0.0021	0.0044	0.0101	0.0067	0.0040	0.0021	0.0010	0.0004
500	0.0019	0.0036	0.0009	0.0032	0.0026	0.0060	0.0146	0.0096	0.0056	0.0029	0.0014	0.0005
510	0.0019	0.0065	0.0013	0.0067	0.0032	0.0077	0.0203	0.0133	0.0078	0.0041	0.0020	0.0007
520	0.0020	0.0096	0.0016	0.0125	0.0036	0.0089	0.0266	0.0174	0.0103	0.0054	0.0026	0.0009
530	0.0020	0.0117	0.0020	0.0188	0.0036	0.0091	0.0320	0.0210	0.0123	0.0065	0.0032	0.0011
540	0.0020	0.0124	0.0022	0.0236	0.0037	0.0083	0.0353	0.0232	0.0136	0.0072	0.0035	0.0012
550	0.0021	0.0122	0.0023	0.0272	0.0042	0.0073	0.0384	0.0252	0.0148	0.0078	0.0038	0.0014
560	0.0022	0.0126	0.0027	0.0324	0.0047	0.0066	0.0443	0.0290	0.0171	0.0090	0.0043	0.0016
570	0.0023	0.0118	0.0032	0.0353	0.0054	0.0057	0.0474	0.0310	0.0184	0.0097	0.0046	0.0017
580	0.0024	0.0104	0.0044	0.0370	0.0073	0.0051	0.0493	0.0322	0.0191	0.0102	0.0048	0.0017
590	0.0025	0.0088	0.0070	0.0390	0.0115	0.0047	0.0514	0.0335	0.0199	0.0106	0.0050	0.0018
600	0.0026	0.0077	0.0127	0.0416	0.0180	0.0046	0.0545	0.0355	0.0211	0.0112	0.0053	0.0019
610	0.0026	0.0067	0.0204	0.0416	0.0242	0.0044	0.0547	0.0354	0.0210	0.0112	0.0053	0.0019
620	0.0025	0.0058	0.0255	0.0391	0.0271	0.0039	0.0513	0.0331	0.0197	0.0104	0.0049	0.0018
630	0.0023	0.0051	0.0265	0.0354	0.0273	0.0035	0.0463	0.0296	0.0176	0.0092	0.0044	0.0016
640	0.0021	0.0045	0.0257	0.0326	0.0276	0.0033	0.0424	0.0271	0.0160	0.0084	0.0040	0.0015
650	0.0019	0.0038	0.0228	0.0282	0.0262	0.0028	0.0366	0.0233	0.0137	0.0072	0.0034	0.0013
660	0.0018	0.0035	0.0211	0.0258	0.0259	0.0027	0.0335	0.0212	0.0124	0.0065	0.0031	0.0011
670	0.0016	0.0031	0.0180	0.0216	0.0231	0.0023	0.0284	0.0179	0.0105	0.0055	0.0026	0.0010
680	0.0014	0.0028	0.0151	0.0173	0.0197	0.0019	0.0235	0.0148	0.0087	0.0045	0.0021	0.0008
690	0.0013	0.0026	0.0132	0.0151	0.0176	0.0017	0.0207	0.0129	0.0076	0.0039	0.0019	0.0007
700	0.0012	0.0023	0.0115	0.0134	0.0154	0.0014	0.0177	0.0111	0.0065	0.0033	0.0016	0.0006
710	0.0011	0.0020	0.0095	0.0115	0.0130	0.0011	0.0147	0.0092	0.0053	0.0027	0.0013	0.0005
720	0.0010	0.0015	0.0078	0.0094	0.0106	0.0009	0.0118	0.0074	0.0043	0.0022	0.0011	0.0004

Table A.2: Spectral measurements of an X-rite Mini ColorChecker (#13 - #24). We first measure the radiance of 24 color patches under static illumination with a spectroradiometer (See Fig. 4.5). And we multiply the transmittance of the LCTF for each channel, yielding the radiance value per wavelength as above. Multiplying the transmittance of the LCTF makes the radiometric calibration robust as it compensates the varying bandwidths of different channels of the LCTF. The numbers in the table correspond to the numbers of the color patches in Fig. 4.5.

A.1.2 Multispectral Camera

Colorchecker camera intensity #1 - #12 [0 - 1]												
Wave-length	#1	#2	#3	#4	#5	#6	#7	#8	#9	#10	#11	#12
440	0.0003	0.0051	0.0106	0.0006	0.0163	0.0135	0.0004	0.0144	0.0043	0.0051	0.0020	0.0013
450	0.0054	0.0225	0.0387	0.0073	0.0567	0.0519	0.0062	0.0522	0.0181	0.0192	0.0117	0.0093
460	0.0067	0.0285	0.0439	0.0086	0.0614	0.0621	0.0074	0.0582	0.0193	0.0189	0.0137	0.0104
470	0.0057	0.0272	0.0375	0.0081	0.0523	0.0596	0.0071	0.0475	0.0160	0.0147	0.0130	0.0099
480	0.0039	0.0246	0.0275	0.0076	0.0376	0.0516	0.0061	0.0305	0.0114	0.0090	0.0128	0.0089
490	0.0064	0.0392	0.0353	0.0117	0.0465	0.0753	0.0098	0.0337	0.0151	0.0106	0.0245	0.0138
500	0.0109	0.0651	0.0505	0.0196	0.0640	0.1168	0.0165	0.0418	0.0229	0.0152	0.0563	0.0231
510	0.0145	0.0811	0.0601	0.0277	0.0761	0.1520	0.0226	0.0455	0.0287	0.0188	0.0987	0.0341
520	0.0234	0.1050	0.0793	0.0534	0.0990	0.2227	0.0423	0.0531	0.0405	0.0246	0.1980	0.0725
530	0.0322	0.1130	0.0938	0.0905	0.1157	0.2740	0.0737	0.0575	0.0517	0.0290	0.2932	0.1580
540	0.0373	0.1210	0.1021	0.1075	0.1291	0.2992	0.0957	0.0597	0.0595	0.0333	0.3483	0.2476
550	0.0421	0.1367	0.1061	0.1081	0.1362	0.3035	0.1144	0.0597	0.0654	0.0382	0.3746	0.3017
560	0.0558	0.1635	0.1165	0.1127	0.1482	0.3301	0.1688	0.0666	0.0803	0.0420	0.4284	0.3804
570	0.0707	0.1858	0.1192	0.1113	0.1520	0.3282	0.2426	0.0696	0.0969	0.0469	0.4500	0.4492
580	0.0823	0.2319	0.1185	0.1083	0.1581	0.2983	0.3257	0.0704	0.1408	0.0555	0.4347	0.4981
590	0.0965	0.3109	0.1206	0.1068	0.1748	0.2599	0.4214	0.0728	0.2470	0.0707	0.3960	0.5408
600	0.1081	0.3663	0.1235	0.1064	0.1894	0.2369	0.4792	0.0759	0.3305	0.0797	0.3667	0.5523
610	0.1170	0.4314	0.1226	0.1047	0.2133	0.2061	0.5290	0.0785	0.4553	0.0933	0.3253	0.5742
620	0.1167	0.4488	0.1152	0.1010	0.2103	0.1818	0.5140	0.0767	0.5057	0.0982	0.2922	0.5582
630	0.1038	0.4005	0.0976	0.0899	0.1851	0.1528	0.4335	0.0681	0.4612	0.0911	0.2498	0.4953
640	0.0996	0.3709	0.0884	0.0826	0.1796	0.1332	0.3814	0.0641	0.4104	0.0845	0.2164	0.4419
650	0.0893	0.3327	0.0810	0.0748	0.1828	0.1145	0.3227	0.0605	0.3603	0.0790	0.1884	0.3882
660	0.0848	0.3160	0.0774	0.0683	0.1904	0.1022	0.2902	0.0617	0.3244	0.0776	0.1718	0.3467
670	0.0699	0.2751	0.0663	0.0565	0.1751	0.0883	0.2431	0.0589	0.2722	0.0732	0.1512	0.2892
680	0.0614	0.2515	0.0583	0.0488	0.1574	0.0809	0.2195	0.0574	0.2405	0.0705	0.1377	0.2560
690	0.0470	0.2137	0.0457	0.0375	0.1304	0.0707	0.1819	0.0564	0.1943	0.0689	0.1191	0.2106
700	0.0372	0.1838	0.0353	0.0294	0.1077	0.0607	0.1521	0.0567	0.1579	0.0685	0.1018	0.1734
710	0.0310	0.1560	0.0271	0.0231	0.0879	0.0481	0.1267	0.0571	0.1264	0.0658	0.0814	0.1383
720	0.0250	0.1241	0.0215	0.0181	0.0714	0.0356	0.0992	0.0531	0.0986	0.0584	0.0617	0.1070

Table A.3: Camera output intensity of an X-rite Mini ColorChecker (#1 - #12). We capture an image of 24 color patches under static illumination with our multispectral camera. (See Fig. 4.5). Each output intensity is averaged for the area of each patch and is normalized to $[0,1]$. The numbers in the table correspond to the numbers of the color patches in Fig. 4.5.

Colorchecker camera intensity #13 - #24 [0 - 1]												
Wave-length	#13	#14	#15	#16	#17	#18	#19	#20	#21	#22	#23	#24
440	0.0099	0.0011	0.0006	0.0018	0.0141	0.0128	0.0403	0.0279	0.0162	0.0077	0.0030	0.0001
450	0.0394	0.0099	0.0075	0.0110	0.0457	0.0496	0.1346	0.0946	0.0570	0.0296	0.0139	0.0042
460	0.0457	0.0126	0.0080	0.0120	0.0448	0.0592	0.1545	0.1070	0.0634	0.0325	0.0152	0.0047
470	0.0375	0.0122	0.0071	0.0110	0.0361	0.0553	0.1342	0.0920	0.0546	0.0279	0.0128	0.0038
480	0.0224	0.0122	0.0055	0.0102	0.0236	0.0454	0.1018	0.0704	0.0418	0.0211	0.0093	0.0026
490	0.0227	0.0237	0.0081	0.0194	0.0273	0.0607	0.1363	0.0930	0.0552	0.0283	0.0130	0.0040
500	0.0253	0.0522	0.0130	0.0468	0.0377	0.0879	0.2077	0.1424	0.0850	0.0443	0.0210	0.0072
510	0.0257	0.0828	0.0172	0.0875	0.0457	0.1073	0.2648	0.1835	0.1104	0.0583	0.0280	0.0099
520	0.0284	0.1424	0.0260	0.1948	0.0573	0.1399	0.3838	0.2684	0.1632	0.0871	0.0425	0.0153
530	0.0306	0.1871	0.0349	0.3255	0.0601	0.1499	0.4976	0.3468	0.2108	0.1130	0.0555	0.0202
540	0.0320	0.2043	0.0401	0.4196	0.0649	0.1424	0.5670	0.3959	0.2404	0.1290	0.0633	0.0231
550	0.0327	0.2022	0.0436	0.4826	0.0742	0.1251	0.6108	0.4270	0.2608	0.1412	0.0695	0.0257
560	0.0384	0.2169	0.0511	0.5860	0.0865	0.1158	0.7444	0.5132	0.3105	0.1673	0.0814	0.0298
570	0.0410	0.2083	0.0620	0.6551	0.0983	0.1037	0.8106	0.5587	0.3413	0.1849	0.0899	0.0329
580	0.0413	0.1829	0.0809	0.6896	0.1313	0.0918	0.8264	0.5764	0.3553	0.1929	0.0923	0.0335
590	0.0423	0.1523	0.1259	0.7094	0.2084	0.0852	0.8499	0.5910	0.3635	0.1980	0.0947	0.0348
600	0.0438	0.1375	0.1852	0.7122	0.2725	0.0807	0.8669	0.5945	0.3634	0.1967	0.0942	0.0349
610	0.0451	0.1168	0.3294	0.7192	0.3980	0.0759	0.8843	0.6004	0.3657	0.1973	0.0947	0.0356
620	0.0440	0.1034	0.4552	0.6972	0.4778	0.0709	0.8494	0.5767	0.3511	0.1887	0.0905	0.0342
630	0.0385	0.0868	0.4672	0.6185	0.4750	0.0620	0.7436	0.5069	0.3083	0.1645	0.0789	0.0298
640	0.0349	0.0741	0.4312	0.5451	0.4633	0.0554	0.6541	0.4399	0.2671	0.1427	0.0692	0.0266
650	0.0311	0.0628	0.3873	0.4827	0.4497	0.0492	0.5723	0.3844	0.2346	0.1250	0.0603	0.0230
660	0.0287	0.0569	0.3514	0.4328	0.4360	0.0453	0.5134	0.3441	0.2092	0.1116	0.0541	0.0206
670	0.0247	0.0499	0.2964	0.3588	0.3821	0.0381	0.4253	0.2860	0.1741	0.0923	0.0446	0.0167
680	0.0224	0.0458	0.2620	0.3096	0.3409	0.0334	0.3775	0.2520	0.1527	0.0806	0.0388	0.0146
690	0.0188	0.0398	0.2137	0.2469	0.2843	0.0265	0.3064	0.2030	0.1228	0.0645	0.0309	0.0114
700	0.0162	0.0340	0.1751	0.2077	0.2377	0.0205	0.2496	0.1650	0.0997	0.0521	0.0248	0.0089
710	0.0142	0.0275	0.1407	0.1716	0.1927	0.0155	0.2016	0.1317	0.0790	0.0408	0.0192	0.0068
720	0.0122	0.0205	0.1102	0.1358	0.1519	0.0122	0.1563	0.1017	0.0607	0.0311	0.0144	0.0047

Table A.4: Camera output intensity of an X-rite Mini ColorChecker (#13 - #24). We capture an image of 24 color patches under static illumination with our multispectral camera. (See Fig. 4.5). Each output intensity is averaged for the area of each patch and is normalized to $[0,1]$. The numbers in the table correspond to the numbers of the color patches in Fig. 4.5.

Appendix B. Multispectral Images

B.1 A Soap

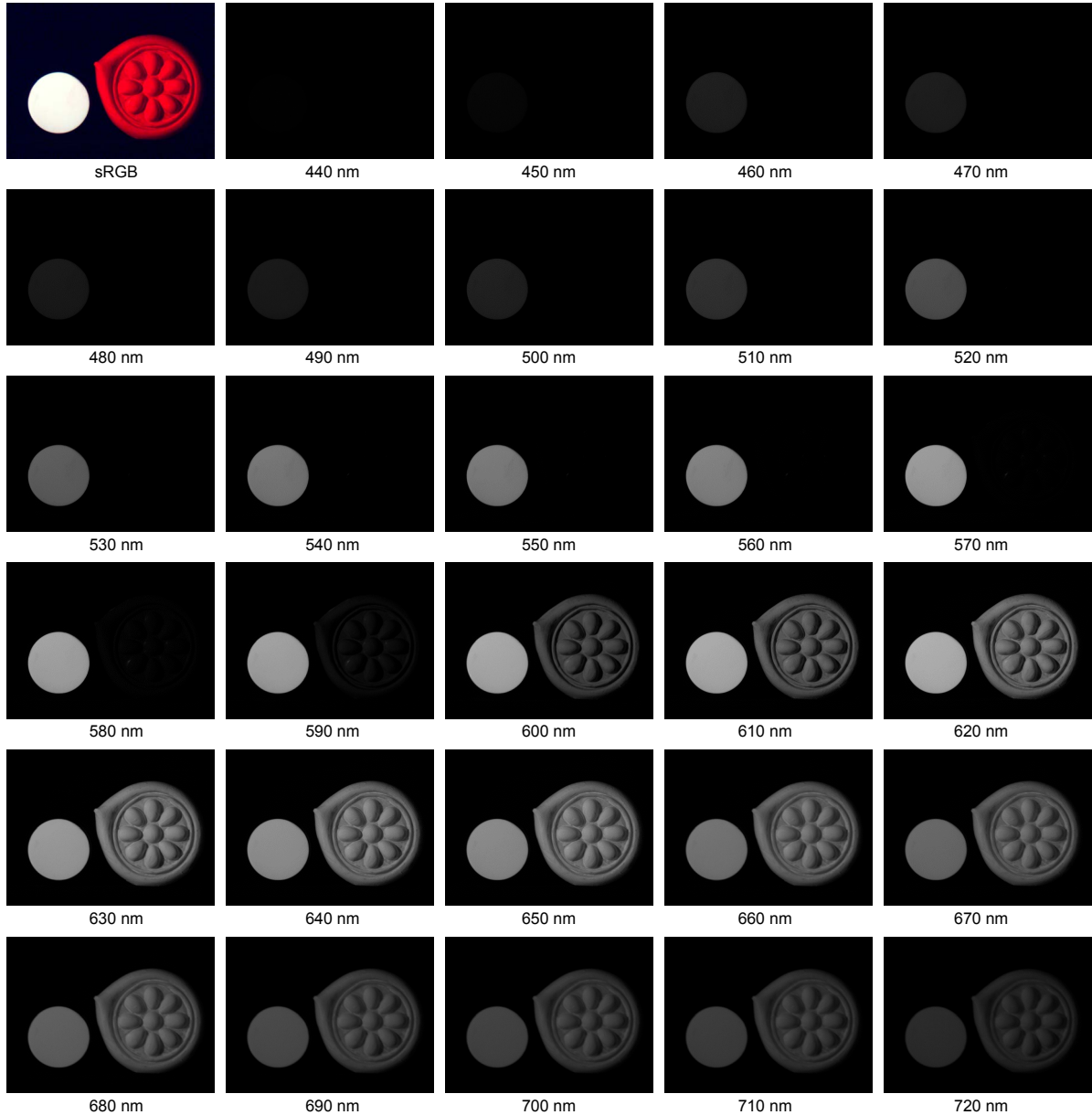


Figure B.1: A multispectral image: a soap with light #1. We store the multispectral reflectance data of multiple channels in a multi-layer OpenEXR file. Each channel stores the reflectance data of corresponding wavelength. This figure presents 29 channels of a multispectral image and its sRGB image.

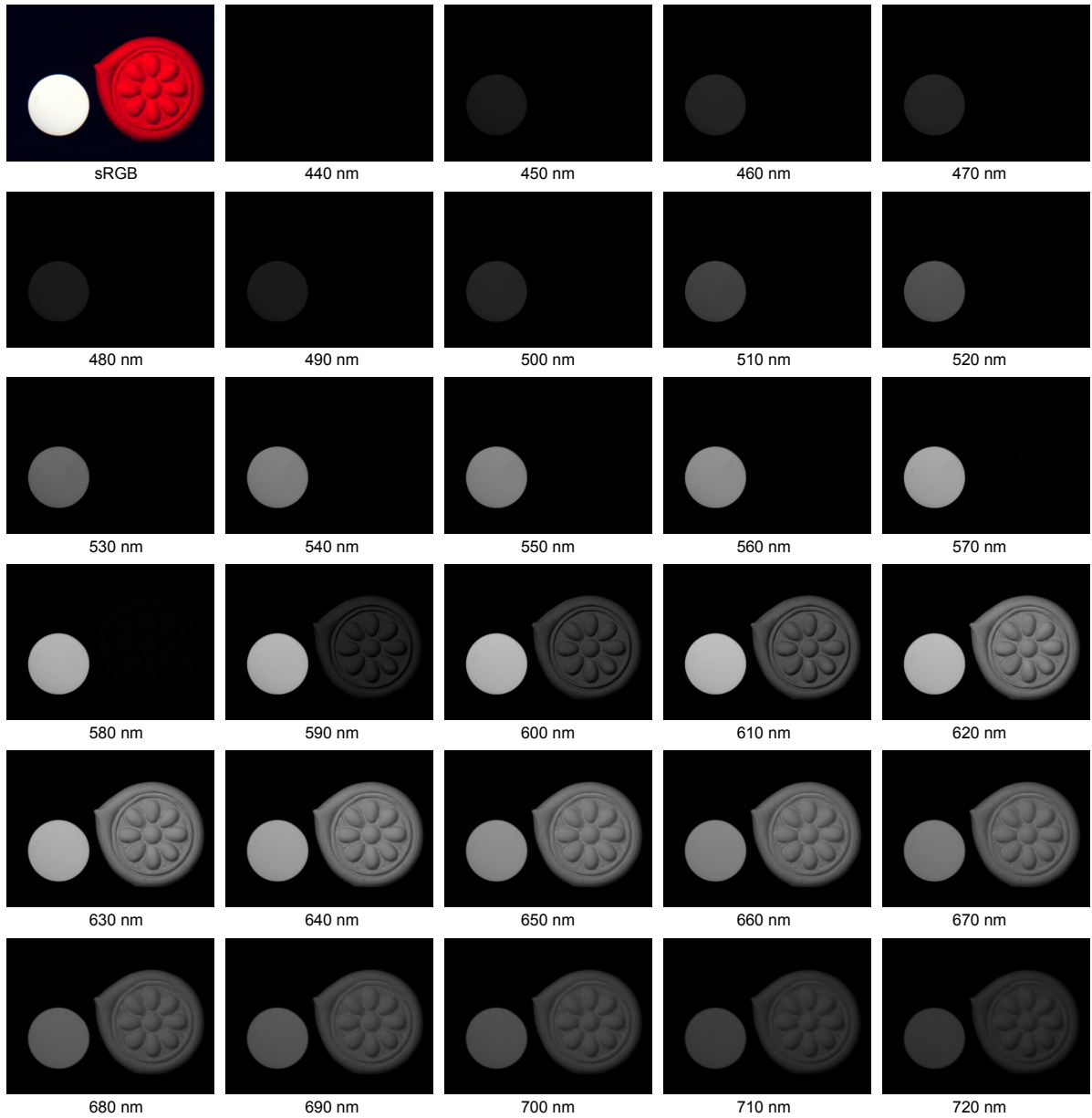


Figure B.2: A multispectral image: a soap with light #2. We store the multispectral reflectance data of multiple channels in a multi-layer OpenEXR file. Each channel stores the reflectance data of corresponding wavelength. This figure presents 29 channels of a multispectral image and its sRGB image.

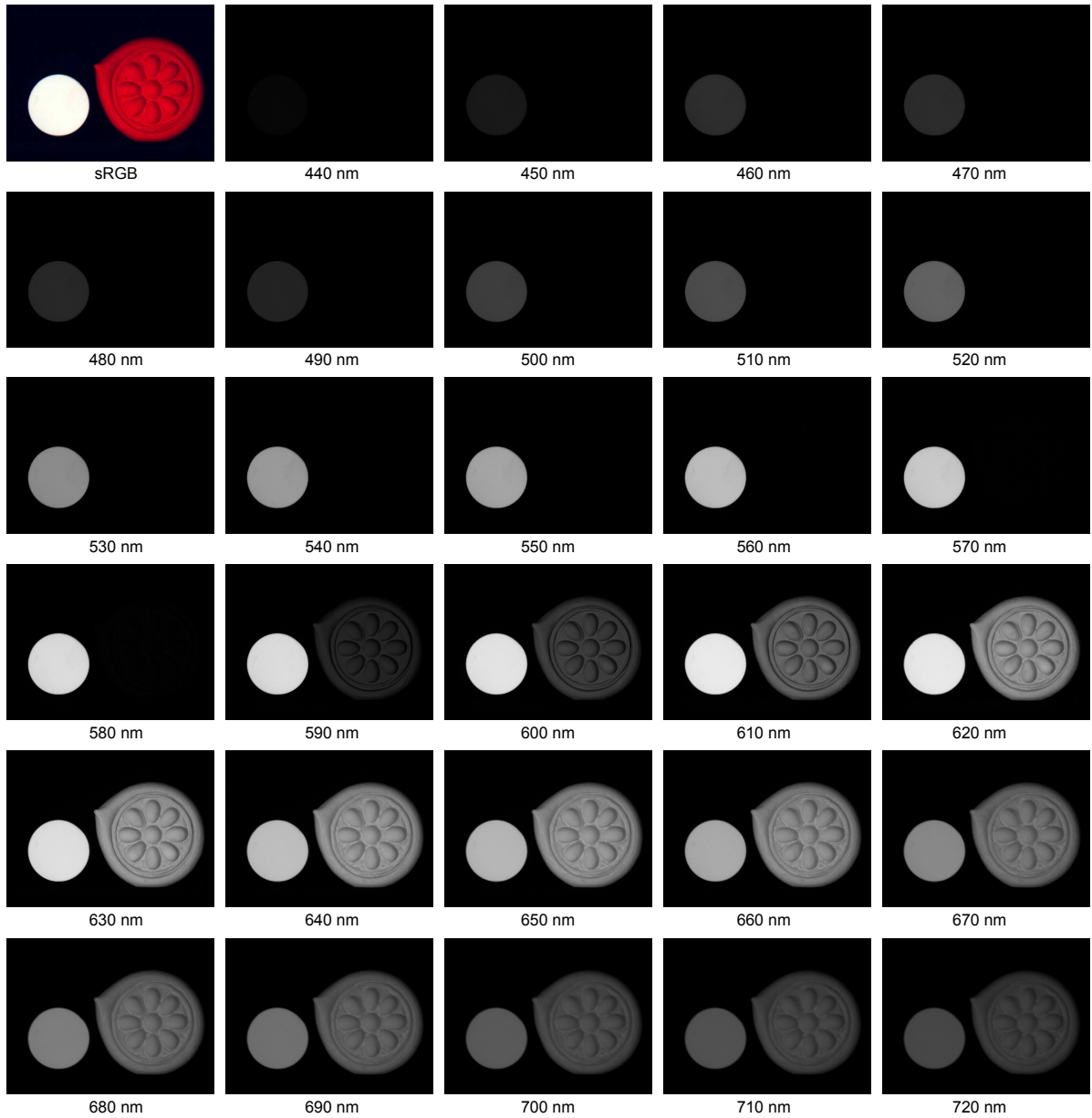


Figure B.3: A multispectral image: a soap with light #3. We store the multispectral reflectance data of multiple channels in a multi-layer OpenEXR file. Each channel stores the reflectance data of corresponding wavelength. This figure presents 29 channels of a multispectral image and its sRGB image.

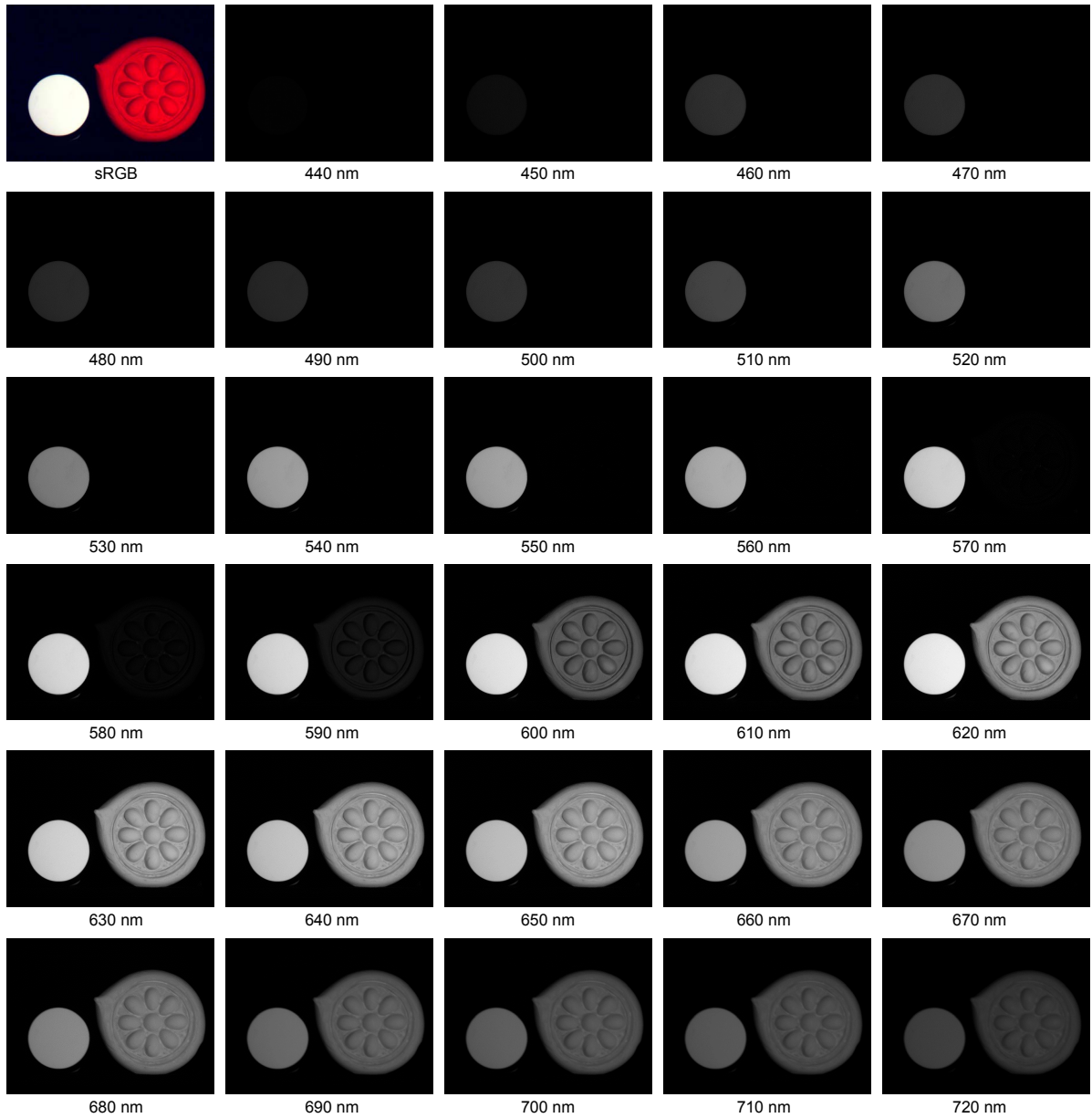


Figure B.4: A multispectral image: a soap with light #4. We store the multispectral reflectance data of multiple channels in a multi-layer OpenEXR file. Each channel stores the reflectance data of corresponding wavelength. This figure presents 29 channels of a multispectral image and its sRGB image.

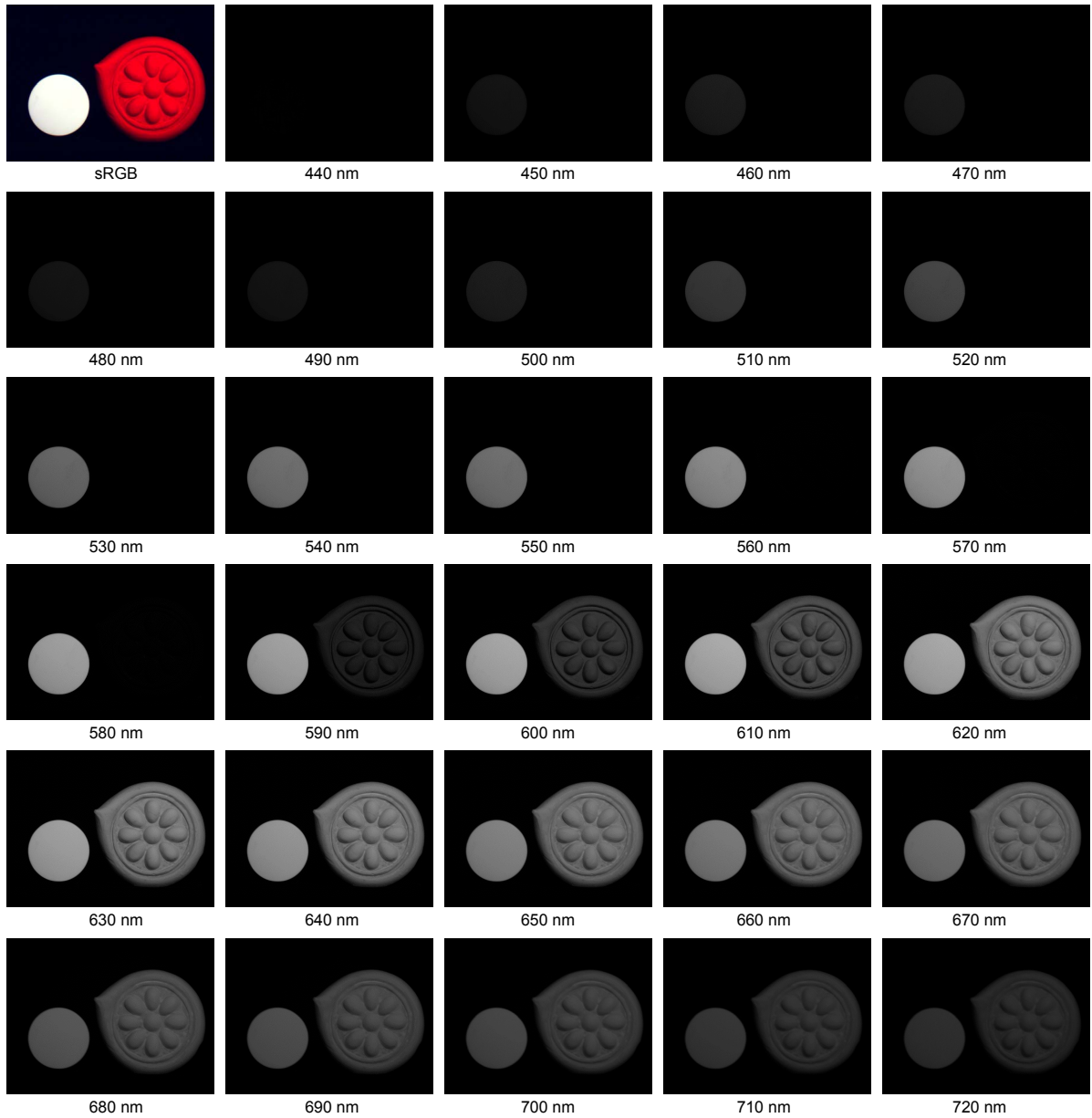


Figure B.5: A multispectral image: a soap with light #5. We store the multispectral reflectance data of multiple channels in a multi-layer OpenEXR file. Each channel stores the reflectance data of corresponding wavelength. This figure presents 29 channels of a multispectral image and its sRGB image.

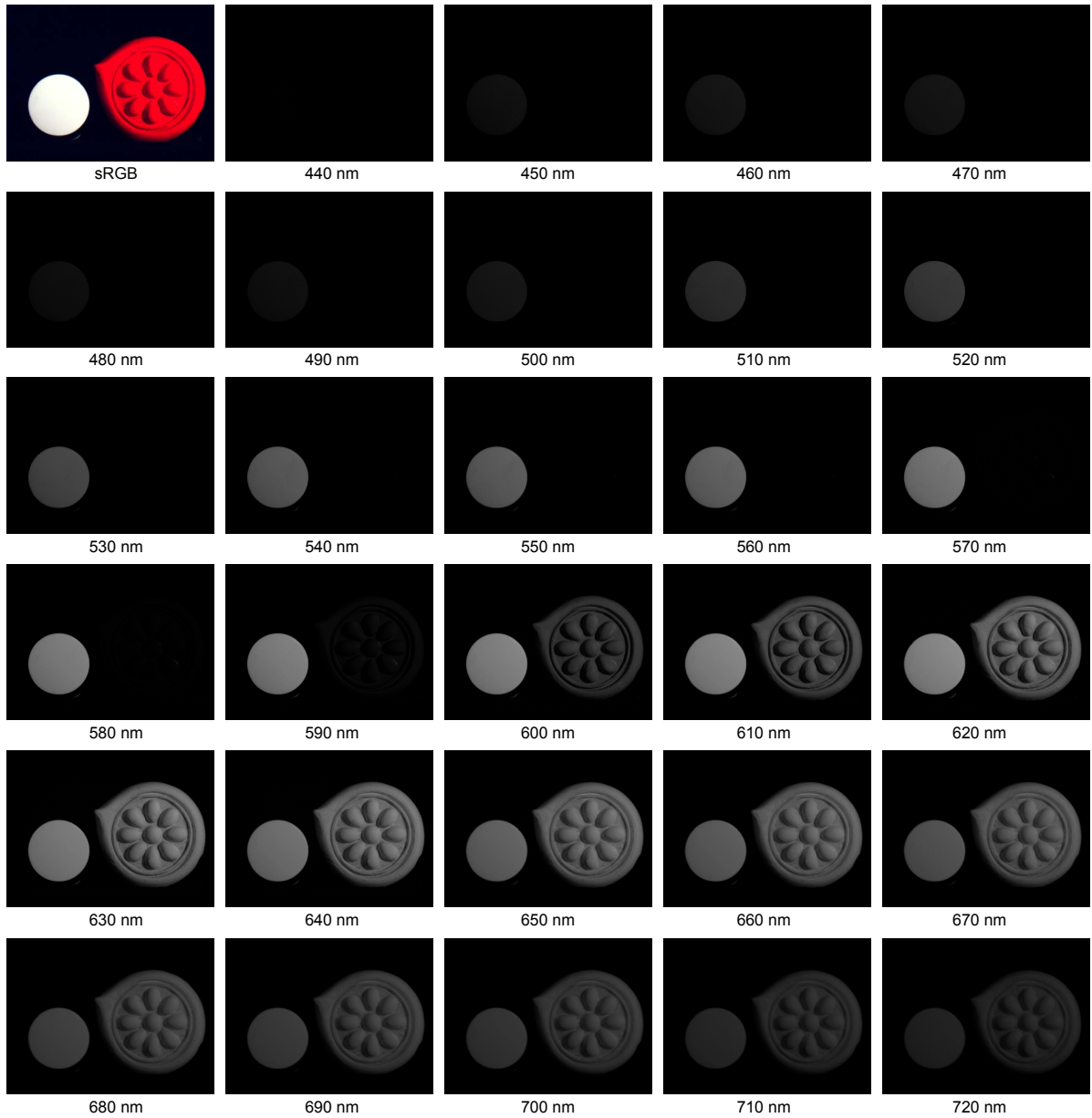


Figure B.6: A multispectral image: a soap with light #6. We store the multispectral reflectance data of multiple channels in a multi-layer OpenEXR file. Each channel stores the reflectance data of corresponding wavelength. This figure presents 29 channels of a multispectral image and its sRGB image.

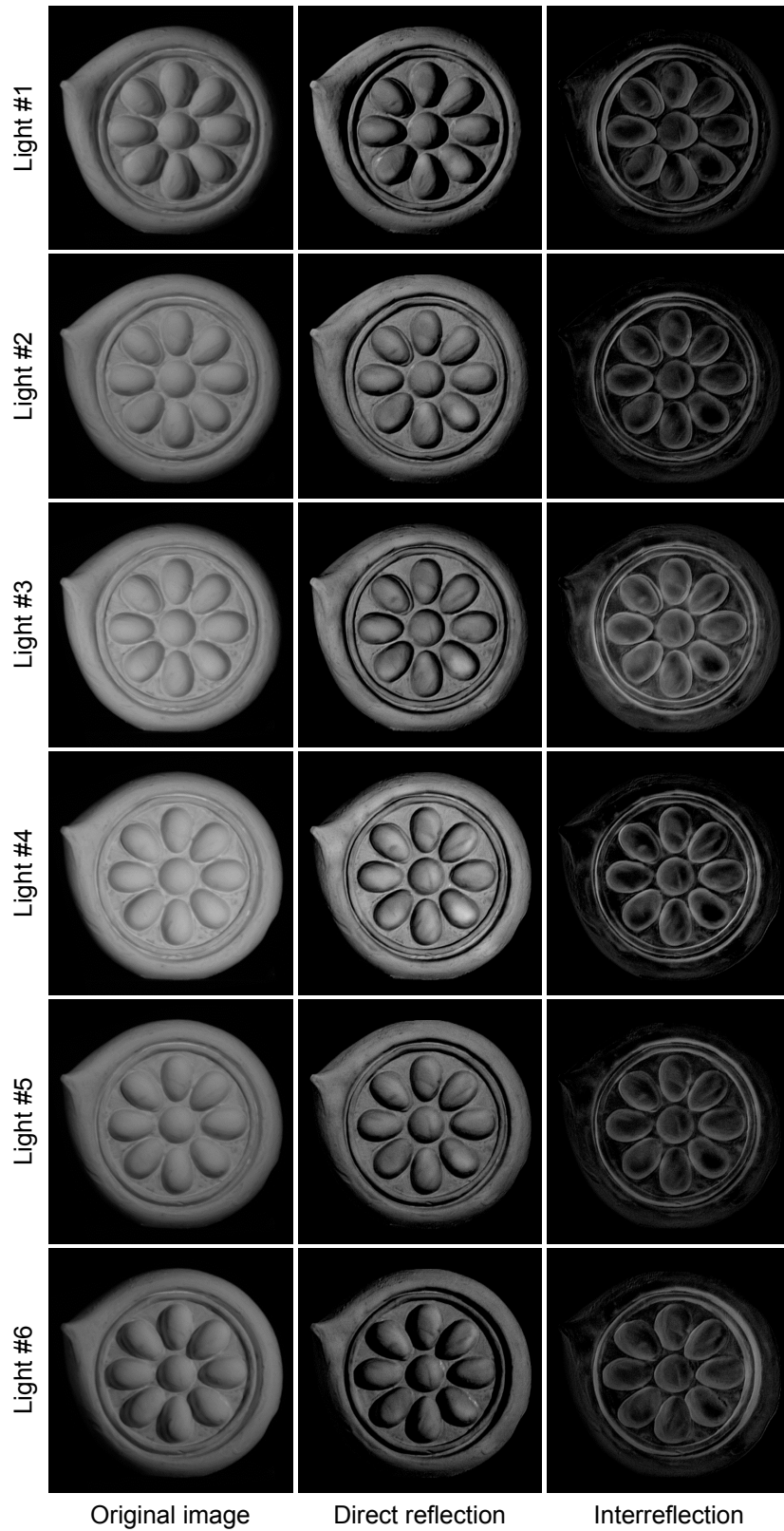


Figure B.7: An example of our interreflection removal algorithm. The left column shows the original images with interreflection. The middle column presents images of direct reflection only. The right column shows the images of interreflection effect. The direct reflection images show sharper edges and shadows compared to the original images. Each row presents the image under each light sources: light #1 - #6.

References

- [1] Michael Attas, Edward Cloutis, Catherine Collins, Douglas Goltz, Claudine Majzels, James R Mansfield, and Henry H Mantsch. Near-infrared spectroscopic imaging in art conservation: investigation of drawing constituents. *Journal of Cultural Heritage*, 4(2):127–136, 2003.
- [2] Svetlana Barsky and Maria Petrou. The 4-source photometric stereo technique for three-dimensional surfaces in the presence of highlights and shadows. *Pattern Analysis and Machine Intelligence, IEEE Transactions on*, 25(10):1239–1252, 2003.
- [3] Ronen Basri, David Jacobs, and Ira Kemelmacher. Photometric stereo with general, unknown lighting. *International Journal of Computer Vision*, 72(3):239–257, 2007.
- [4] Gabriel J Brostow, Carlos Hernández, George Vogiatzis, Björn Stenger, and Roberto Cipolla. Video normals from colored lights. *Pattern Analysis and Machine Intelligence, IEEE Transactions on*, 33(10):2104–2114, 2011.
- [5] Manmohan Chandraker, Sameer Agarwal, and David Kriegman. Shadowcuts: Photometric stereo with shadows. In *Proc. IEEE Conference on Computer Vision and Pattern Recognition (CVPR)*, pages 1–8. IEEE, 2007.
- [6] Hao Du, Xin Tong, Xun Cao, and Stephen Lin. A prism-based system for multispectral video acquisition. In *Proc. IEEE 12th International Conference on Computer Vision (ICCV)*, pages 175–182. IEEE, 2009.
- [7] Jinwei Gu, Toshihiro Kobayashi, Mohit Gupta, and Shree K Nayar. Multiplexed illumination for scene recovery in the presence of global illumination. In *Proc. IEEE International Conference on Computer Vision (ICCV)*, pages 691–698. IEEE, 2011.
- [8] Mohit Gupta and Shree K Nayar. Micro phase shifting. In *Proc. IEEE Conference on Computer Vision and Pattern Recognition (CVPR)*, pages 813–820, 2012.
- [9] Ralf Habel, Michael Kudenov, and Michael Wimmer. Practical spectral photography. *Computer Graphics Forum*, 31(2pt2):449–458, 2012.
- [10] Carlos Hernández, George Vogiatzis, and Roberto Cipolla. Shadows in three-source photometric stereo. In *Proc. European Conference on Computer Vision (ECCV)*, pages 290–303. Springer, 2008.

- [11] Cambridge Research & Instrumentation Inc. *CRi VariSpec Liquid Crystal Tunable Filters SDK*. <http://www.spectralcameras.com/varispec>.
- [12] Point Grey Research Inc. *Point Grey FlayCapture[®] SDK*. <http://ww2.ptgrey.com/sdk/flycap>.
- [13] Wenzel Jakob. Mitsuba renderer, 2010. <http://www.mitsuba-renderer.org>.
- [14] James T Kajiya. The rendering equation. In *Proc. ACM SIGGRAPH Computer Graphics*, volume 20, pages 143–150, 1986.
- [15] Rei Kawakami, John Wright, Yu-Wing Tai, Yasuyuki Matsushita, Moshe Ben-Ezra, and Katsushi Ikeuchi. High-resolution hyperspectral imaging via matrix factorization. In *Proc. IEEE Conference on Computer Vision and Pattern Recognition (CVPR)*, pages 2329–2336. IEEE, 2011.
- [16] Min H. Kim, Todd Alan Harvey, David S. Kittle, Holly Rushmeier, Julie Dorsey, Richard O. Prum, and David J. Brady. 3D imaging spectroscopy for measuring hyperspectral patterns on solid objects. *ACM Transactions on Graphics (Proc. SIGGRAPH 2012)*, 31(4):38:1–11, 2012.
- [17] Jan J Koenderink and AJ Van Doorn. Geometrical modes as a general method to treat diffuse interreflections in radiometry. *Journal of the Optical Society of America (JOSA)*, 73(6):843–850, 1983.
- [18] Haebom Lee and Min H. Kim. Building a two-way hyperspectral imaging system with liquid crystal tunable filters. In *Springer LNCS 8509 (Proc. ICISP 2014)*, pages 26–34, Normandy, France, 2014. Springer.
- [19] Miao Liao, Xinyu Huang, and Ruigang Yang. Interreflection removal for photometric stereo by using spectrum-dependent albedo. In *Proc. IEEE Conference on Computer Vision and Pattern Recognition (CVPR)*, pages 689–696, 2011.
- [20] Lucas Digital Ltd. *Reading and writing OpenEXR image files with the IlmImf library*. <http://www.openexr.com/ReadingAndWritingImageFiles.pdf>, 2006.
- [21] Emilio Marengo, Marcello Manfredi, Orfeo Zerbinati, Elisa Robotti, Eleonora Mazzucco, Fabio Gosetti, Greg Bearman, Fenella France, and Pnina Shor. Development of a technique based on multi-spectral imaging for monitoring the conservation of cultural heritage objects. *Analytica chimica acta*, 706(2):229–237, 2011.
- [22] MATLAB. *version 8.3 (R2014a)*. The MathWorks Inc., Natick, Massachusetts, 2014.
- [23] Jean-Pierre Mohen, Michel Menu, and Bruno Mottin. *Mona Lisa: inside the painting*. Abrams, 2006.

- [24] Pantazis Mouroulis, Robert O Green, and Thomas G Chrien. Design of pushbroom imaging spectrometers for optimum recovery of spectroscopic and spatial information. *Applied Optics*, 39(13):2210–2220, 2000.
- [25] Shree K Nayar, Katsushi Ikeuchi, and Takeo Kanade. Shape from interreflections. *International Journal of Computer Vision (IJCV)*, 6(3):173–195, 1991.
- [26] Shree K Nayar, Gurunandan Krishnan, Michael D Grossberg, and Ramesh Raskar. Fast separation of direct and global components of a scene using high frequency illumination. *ACM Transactions on Graphics (TOG)*, 25(3):935–944, 2006.
- [27] Konstantinos Rapantzikos and Costas Balas. Hyperspectral imaging: potential in non-destructive analysis of palimpsests. In *Proc. IEEE International Conference on Image Processing (ICIP)*, volume 2, pages II–618. IEEE, 2005.
- [28] Jiuai Sun, Melvyn Smith, Lyndon Smith, Sagar Midha, and Jeff Bamber. Object surface recovery using a multi-light photometric stereo technique for non-lambertian surfaces subject to shadows and specularities. *Image and Vision Computing*, 25(7):1050–1057, 2007.
- [29] Tsuyoshi Takatani, Yasuyuki Matsushita, Stephen Lin, Yasuhiro Mukaigawa, and Yasushi Yagi. Enhanced photometric stereo with multispectral images. In *Proc. International Conference on Machine Vision Applications (MVA)*. IAPR, 2013.
- [30] Frank Verbiest and Luc Van Gool. Photometric stereo with coherent outlier handling and confidence estimation. In *Proc. IEEE Conference on Computer Vision and Pattern Recognition (CVPR)*, pages 1–8, 2008.
- [31] George Vogiatzis and Carlos Hernández. Self-calibrated, multi-spectral photometric stereo for 3d face capture. *International Journal of Computer Vision (IJCV)*, 97(1):91–103, 2012.
- [32] Tai-Pang Wu, Kam-Lun Tang, Chi-Keung Tang, and Tien-Tsin Wong. Dense photometric stereo: A markov random field approach. *Pattern Analysis and Machine Intelligence, IEEE Transactions on*, 28(11):1830–1846, 2006.
- [33] Insu Yu, Andrew Cox, Min H. Kim, Tobias Ritschel, Thorsten Grosch, Carsten Dachsbacher, and Jan Kautz. Perceptual influence of approximate visibility in indirect illumination. *ACM Transactions on Applied Perception (Presented at APGV 2009)*, 6(4):24:1–24:14, 2009.

Summary

Developing a Multispectral Photometric Stereo System for Acquiring High-Fidelity Surface Normals

다분광 이미징 기법은 촬영 피사체의 물리적 휘도값을 측정하는 용도로 널리 쓰여지고 있다. 포토메트릭 스테레오 기법은 물체의 3차원 모양을 디지털화하는 기법으로, 지난 30년간 많은 분야에서 활용되어왔다. 하지만 이 두가지 기법이 3차원 이미징 응용분야에서 융합되어 쓰인 적은 거의 없다. 포토메트릭 스테레오 기법을 이용해서 물체의 3차원 모양을 측정하는 것에는 여러가지 방해물들이 있다. 예를 들어, 물체 표면에서의 상호반사, 거울반사, 그림자 등의 광학 현상들은 포토메트릭 스테레오의 근본 가정인 표면 난반사를 방해하는 현상들이다. 특히, 물체 표면에서의 상호반사를 제거하는 것은 굉장히 까다로운 일이다. 왜냐하면, 상호반사를 제거하기 위해서는 물체의 3차원 정보가 필요하고, 물체의 3차원 정보는 우리 측정하고자 하는 최종 목표이기 때문이다. 우리는 이 논문에서 난반사 조건하에 물체 표면의 상호반사를 제거하기 위한 획기적인 다분광 포토메트릭 스테레오 시스템을 소개한다. 우리는 상호반사를 수학적으로 모델링하고, 다분광 이미징 기법을 이용하여 측정된 휘도값에서부터 상호반사를 제거하고, 직접반사를 측정함으로써 기존의 포토메트릭 스테레오 시스템의 성능을 향상시킨다. 우리가 제안하는 시스템의 방사 보정 및 기하학적 보정 과정을 자세히 설명한다. 또한 우리가 제안하는 시스템의 3차원 측정 효과의 정확성에 대하여 정량적, 정석적 비교 분석을 제공한다.

감 사 의 글

제가 이 석사 학위 논문을 쓰기까지 도움을 주신 모든 분들께 감사의 말을 전합니다. 먼저, 멀리 떨어져 있으면서도 항상 아들을 믿고 지지해주시는 어머니, 아버지에게 평소 표현하지 못한 무한한 감사와 사랑의 말을 전하고 싶습니다. 자주 보지는 못하지만 세상에서 하나뿐인 누나에게도 고마움을 전합니다.

대학원 입학부터 석사 졸업까지 가장 많은 시간을 함께한 주호와 기꺼이 제 실험의 촬영 대상이 되어준 인창이에게도 고마움을 표합니다. 항상 열정적이고 의욕적인 승환이, 묵묵히 할 일을 잘 해내는 해봄이, 바로 옆자리에서 매일 얼굴 마주보는 영범이에게도 고마움을 전하고 싶습니다. 서로의 힘든 대학원 생활을 다독여주며 버팀목이 되어준 친구 정빈이, 미국에 있으면서도 변함없는 우정을 나누고 있는 요섭이에게도 고마움을 느낍니다.

특히, 2년동안 저에게 연구의 하나부터 열까지를 가르쳐 주신 저의 지도교수님, 김민혁 교수님께 감사드립니다. 교수님의 열성적인 지도로 저 또한 과학적 연구라는 것에 더욱 흥미를 가지게 되었고, 직업으로서의 학문에 대해 생각해보게 되었습니다. 카이스트 비주얼 컴퓨팅 연구실의 창립멤버로서 교수님의 첫번째 제자로 석사 학위를 받아 영광입니다.

이외에도 언급하지 못한 제 주위의 모든 분들께 살아가면서 많은 도움을 받았습니다. 저의 이 작은 결실이 그분들께 조금이나마 보답이 되기를 바랍니다